CHARACTERIZATION OF TWO CARBON-SIXTY SYSTEMS: ELECTRON-DOPED
CARBON-SIXTY MONOLAYERS ON THIN-FILM METAL UNDERLAYERS, AND
COMPOSITE FILMS OF CARBON-SIXTY AND NICKEL

By

QUENTIN M. HUDSPETH

A DISSERTATION PRESENTED TO THE GRADUATE SCHOOL OF THE
UNIVERSITY OF FLORIDA IN PARTIAL FULFILLMENT OF THE
REQUIREMENTS FOR THE DEGREE OF DOCTOR OF PHILOSOPHY

UNIVERSITY OF FLORIDA

2001

I dedicate this dissertation to my beloved wife.  Without her I would be lost.


Thank you Heather.  You make my life amazing.

## ACKNOWLEDGEMENTS

I would like to take this opportunity to thank all those who have helped me realize my dream: the members of my committee for their guidance and support; my advisor, Dr. Art Hebard, for taking a chance on me; the members of my research group who are the best people I have ever had the pleasure to work with; and the staff here at the Department of Physics, who deserve more praise than they ever get.

I give special thanks to Dr. Steve Arnason, my second advisor, for many wonderful conversations, some of which were even about physics. I am indebted to Partha Mitra for his fitting of my weak localization data. I thank Drs. Art Hebard, Jeff Lynn, Steve Arnason, and Mark Meisel for their critical readings of this dissertation. I thank the members of the physics machine shop: Mr. Marc Link, Mr. Bill Malphurs, Mr. Ed Storch, Mr. Ted Melton, Mr. John VanLeer, Mr. Stephen Griffin, and Mr. Bob Fowler. I definitely could not have done it without them. I thank Ms. Janet Germany, Ms. Susan Rizzo, and Ms. Darlene Latimer, for keeping me in line.

I must also thank my family, new and old, for all their support, confidence, and love; for never doubting I could do it, even when I did.

# TABLE OF CONTENTS

LIST OF FIGURES

CHARACTERIZATION OF TWO CARBON-SIXTY SYSTEMS: ELECTRON-DOPED
CARBON-SIXTY MONOLAYERS ON THIN-FILM METAL UNDERLAYERS, AND
COMPOSITE FILMS OF CARBON-SIXTY AND NICKEL

By

Quentin M. Hudspeth

May 2001

Chairman: Dr. Arthur Hebard

Major Department: Physics

A series of transport measurements on thin $C_{60}$/Metal bilayer films and $C_{60}$:$Ni_x$

composite films is presented. $C_{60}$/Metal bilayer films were grown by sequential

deposition of a metal underlayer, followed by 2–3 monolayers of $C_{60}$. The resistance of

the system was measured *in situ* using standard four-terminal measurement techniques.

From the difference in total resistance before and after the deposition of the $C_{60}$ overlayer,

the resistance of the electron-doped monolayer of $C_{60}$ in contact with the metal underlayer

was determined. A sequence of such growth and measurement was performed and the

resistance of $C_{60}$ monolayers doped by contact with both nickel and copper was

determined. Further *ex situ* measurements were conducted on one $C_{60}$/Cu film at low

temperatures and high magnetic fields, from which the weak localization parameters $\alpha$, $P$ and $L_\phi$, were determined for the system.

$C_{60}:Ni_x$ composite films were grown by the simultaneous deposition of nickel and $C_{60}$. *Ex situ* transport measurements were performed on three such films of x = 21, 23, and 90, as well as on one pure nickel film. Nominal stoichiometry was controlled by the relative deposition rates of the nickel and $C_{60}$. As temperature was lowered below 200K, these composite films exhibited a change in magnetoresistance from negative to positive. In contrast, the magnetoresistance of the pure nickel film was negative at all temperatures in the measured range of 5–300K. From anomalous Hall effect measurements, it was shown that the composites remained ferromagnetic even in regions of positive magnetoresistance. A similar crossover was recently reported in $Fe_{1-x}Co_xSi$, which was attributed to the Coulomb interaction enhanced by quantum interference effects. The similarities between $C_{60}:Ni_x$ and $Fe_{1-x}Co_xSi$—insulating, electron correlated host, magnetic dopants—suggest a similar mechanism for the crossover in $C_{60}:Ni_x$.

## CHAPTER 1
## INTRODUCTION

Since Kroto et al.[1] confirmed the existence of the carbon-sixty ($C_{60}$) molecule in

1985, significant research has been undertaken to understand the basic properties and

characteristics of these fascinating molecules as well as to discover technological uses for

them. The quest for technological uses continues, but in many respects, $C_{60}$ is still a

young molecule, so our basic understanding is progressing rapidly.

This dissertation reports on a study of the electrical properties of $C_{60}$ in contact

with a metal. The study follows two lines. First is the examination of a monolayer of $C_{60}$

deposited on the surface of a thin metal film ($C_{60}$/M, where M is nickel or copper).

Second is the measurement of the properties of composite films of $C_{60}$ co-deposited with

nickel ($C_{60}$:$Ni_x$). This dissertation was motivated by work previously completed by

Hebard et al.[2] at Bell Laboratories on $C_{60}$/Cu bilayer systems.

The physics of electronic transport in thin metallic films is a question of length

scales. For a thin enough material, the electrons carrying current begin to behave as if

they are constrained to move only in a single plane. Such a system can be considered

two-dimensional (2D), even though it still has a thickness. Electrons in a 2D system

behave differently than those in a three-dimensional (3D) system. Many properties—

such as the dependence of resistance on temperature or applied magnetic fields—change

as a material undergoes a transition from 2D to 3D. The purpose of this research is to

examine the physics of electron-doped $C_{60}$ in the 2D bilayer system, and in the 3D composite system. This goal is accomplished by studying the electron doping of $C_{60}$ on a variety of metals, and performing transport measurements from 2–300 K and in magnetic fields up to 7 T. Of primary interest are the effects of changing such system features as the work function of the metal, the thickness of the underlayer, and the magnetic properties of the metal underlayer.

When a monolayer of $C_{60}$ is deposited on the surface of a metal film, the high electron affinity of $C_{60}$ facilitates the transfer of electrons from the metal to the overlying monolayer. These transferred electrons are delocalized—free to move about the monolayer—with a mean free path that may be larger than the diameter of the molecule, and hence larger than the thickness of the monolayer. Because the transferred electrons are constrained to move about a single monolayer of $C_{60}$ (on the order of 10 Å thick) the system is effectively 2D and its electronic transport may reveal many interesting and useful properties.

Typical transport measurements of resistance (R), magnetoresistance, and the Hall effect, measured as a function of temperature (T), are used to characterize these films. From the functional form of the R versus T curve, the type of interactions of the current carrying electrons can be extracted. Magnetoresistance, the change in a material's electrical resistance in the presence of an applied magnetic field, is affected by many factors, such as the shape of the Fermi surface and the kinds of scattering the electrons undergo. The Hall effect is the buildup of a voltage across a material perpendicular to the current flow, due to the application of an external magnetic field. From measurements of

the Hall effect as a function of the applied field, the density of electrons available to carry current, as well as their mobility, can be determined.

The difficulty lies in extracting the relevant information from the combined properties of the 2D conducting monolayer and the 3D underlying metal film. One method of extracting such information is to monitor the resistance of the $C_{60}$/M system during the deposition of the monolayer. From the change in resistance as the system goes from a pure metal to a $C_{60}$/M bilayer, the intrinsic resistance of the electron-doped $C_{60}$ monolayer can be calculated. More properties of the conducting monolayer can be observed by examining the difference between the behavior of the $C_{60}$/M system as a function of temperature and applied magnetic field, and the behavior of the metal film alone under the same conditions.

The same measurements are used in the study of composite films of $C_{60}$ and nickel. This system is prepared in the same way as the $C_{60}$/M system, except that nickel and $C_{60}$ are deposited simultaneously onto the same substrate, instead of in sequential layers. Unlike the conducting $C_{60}$ monolayer, these films remain in the 3D regime. The goal is to study the impact of $C_{60}$ on the electrical and magnetic properties of nickel. By comparing the magnetoresistance signature of $C_{60}$:$Ni_x$ composites to that of pure nickel films and to theories explaining magnetoresistance, an understanding of what is happening inside the composite can be formed.

This dissertation presents and discusses the results of these experiments and their impact on our understanding of the physics of electron-doped $C_{60}$ in the 2D bilayer system, and in the 3D composite system.

CHAPTER 2
REVIEW OF DOPED $C_{60}$

Prior to 1985, there were only three known forms of carbon: amorphous carbon, graphite, and diamond. Several workers from as far back as 1966 and as recently as 1981 had theorized the existence of a fourth form of carbon; however, it had yet to be discovered. In 1984 Rohlfing et al.[3] reported a startling discovery while working with photoionization measurements of carbon clusters. For clusters of forty or more carbon atoms, only clusters with an even number of atoms were being generated. In 1985, Kroto et al. confirmed the existence and stability of $C_{60}$, a representative of the fourth known form of carbon, buckminsterfullerene.[1] Buckminsterfullerenes (or fullerenes) are named after architect Buckminster Fuller, who advocated the use of geodesic structures in modern building design. These cage-like molecules are constructed of carbon atoms arranged on a geodesic surface. $C_{60}$, known affectionately as the Buckyball, consists of sixty carbon atoms placed at the vertices of a truncated icosahedron (or soccer ball) structure (Figure 2.1).

The symmetry and associated electronic structure of the $C_{60}$ molecule provide for some interesting properties, such as a high electron affinity (approximately 2.65 eV) and a smooth, narrow band structure.[4] A high electron affinity implies that it is energetically favorable for electrons near the surface of a metal, or for electrons of atoms nestled in the interstitial sites of solid $C_{60}$, to transfer to any $C_{60}$ molecule in contact with the metal.
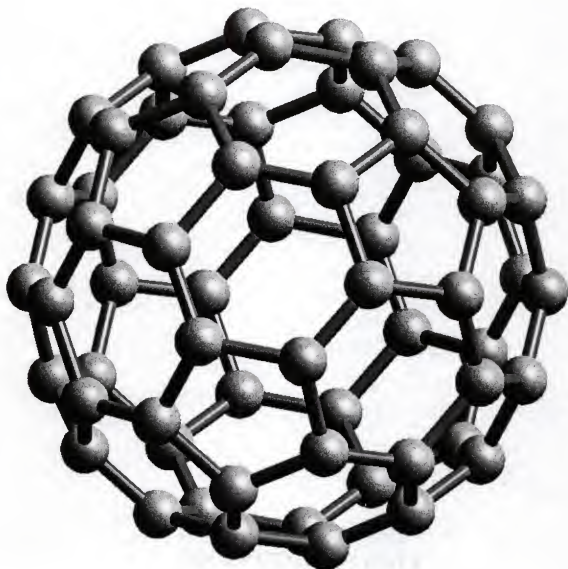
Figure 2.1    Carbon-sixty ($C_{60}$) molecule. The carbon atoms sit at the vertices of a truncated icosahedron. The single-bond length for the pentagons is 1.45 Å, and the double-bond length for the shared edges of the hexagons is 1.40 Å. The cage diameter is 7 Å. For a review see Reference 4

$C_{60}$'s Fermi energy lies between the conduction and valence bands; therefore, it is a semiconductor in its solid state. Transferred electrons populate the triply degenerate Lowest Unoccupied Molecular Orbital (LUMO) of the $C_{60}$ molecule, which may hold up to six electrons. Section 2.1 provides a brief overview of the salient features of the intercalant-doped system.

A second method of electron transfer to $C_{60}$ is through the deposition of a monolayer of $C_{60}$ directly onto a metal surface ($C_{60}$/M, M = any metal). In this case, only $C_{60}$ molecules in direct contact with the metal participate in the electron transfer. Since metal atoms do not diffuse into the interstitial sites of the $C_{60}$, this method is referred to as electron-doping. Although the spectroscopic[5-13] properties of such systems have been well researched, the electrical properties have not. Section 2.2 provides an overview of the salient features of the $C_{60}$/M system.

## 2.1   Bulk, Intercalant-doped $C_{60}$

$C_{60}$ crystals have been doped by intercalating metals into the interstitial sites of the lattice. The spectroscopic[14-18] and transport[4, 19-29] properties of bulk, intercalant-doped $C_{60}$ have been researched extensively, and are reviewed in sections 2.1.1 and 2.1.2, respectively.

The alkali metals most easily form compounds with $C_{60}$. In the vapor phase, they readily diffuse into the interstitial sites of a $C_{60}$ crystal or film. Except for some alkaline earths (Ca, Ba, Sr) and a few rare earths (Yb, Er, Eu, Sm, La, Nd), attempts to form stable compounds with other metals as intercalates have failed. The transition metals, unlike the alkali metals, have a high cohesive energy, which prevents the ready diffusion of atoms into the $C_{60}$ interstitial sites. To estimate roughly whether a metal may form a compound

with $C_{60}$, Wertheim and Buchanan have worked out a rule-of-thumb calculation using the work function of the metal, $e\phi$, the metal's cohesive energy, $E_{coh}$, and the energy of the LUMO of $C_{60}$.[11] They define the intercalation energy to be $E_{intc} = E_{LUMO} - e\phi - E_{coh}$. For positive $E_{intc}$, the metal is likely to form a compound, since it either diffuses easily (low $E_{coh}$) or has a small work function and may therefore be more likely to give up electrons to $C_{60}$'s LUMO. Based on calculated values of $E_{intc}$, few metals should form stable compounds with $C_{60}$. However, $E_{intc}$ gives only a rough estimate of the possibility of compound formation.

### 2.1.1 Spectroscopic Measurements

Theory predicts that the Raman active $A_g(2)$ vibrational mode (Figure 2.2) of $C_{60}$ is charge dependent. This mode is surface-tangential, with the pentagonal areas shrinking as the hexagonal areas expand. Charge added to the $C_{60}$ goes into the anti-bonding orbitals, weakening the effective spring constant of the $A_g(2)$ oscillations. Any charge transfer to the $C_{60}$ would show up as a shift to lower frequency of the $A_g(2)$ Raman peak. Other modes are also expected to be charge dependent, but $A_g(2)$ should have one of the most intense Raman peaks and be one of the peaks most sensitive to changes in the charge state of the molecule. Indeed, many studies (for example, references [23, 30, 31]) have shown that the $A_g(2)$ mode is one of the highest Raman peaks. It is sensitive to charge transfer and shifts approximately 6–8 cm$^{-1}$ for each electron transferred.

Photoemission has also been used to detect charge transfer effects in $A_xC_{60}$ (A = alkali metal).[14-16, 32] Photoemission studies effectively map out the occupied density of states (DOS) at the surface of a material.[33] For molecular solids, like $C_{60}$, the peaks near
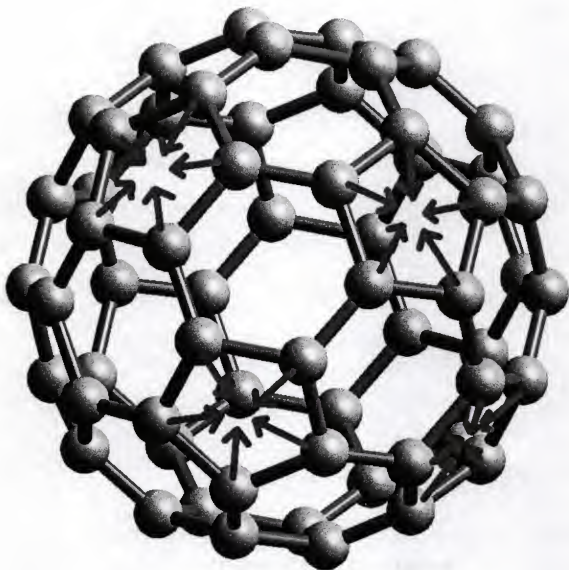
Figure 2.2    Schematic of $A_g(2)$ "pentagonal pinch" vibrational mode. The mode is surface-tangential, with the pentagonal areas shrinking as the hexagonal areas expand, and vice versa. The $A_g(2)$ mode is highly sensitive to charge transfer, and its Raman peak shifts ~6–8 cm$^{-1}$ to lower frequency for every transferred electron.[24, 31, 32]

the Fermi energy correspond to the Highest Occupied Molecular Orbital (HOMO), the next highest (HOMO+1), etc. During doping with an alkali metal, the development of a LUMO-derived peak is observed, as the LUMO begins to fill with transferred electrons. The peak grows continuously with x, reaching a maximum at x = 6.

Photoemission can also indicate whether a material is metallic, since there will be a cutoff in the DOS at the Fermi energy—called the Fermi edge—in the shape of the Fermi function. For an insulator, there is no Fermi edge, as there is no Fermi surface. During exposure to alkali metal vapor, the photoemission spectra for $C_{60}$ develops a definite Fermi edge as x approaches 3, which then disappears as x approaches 6. It should be pointed out that other spectroscopic analyses, such as high-resolution electron energy loss spectroscopy,[33] inverse photoemission spectroscopy,[14] and X-ray absorption spectroscopy, have also been performed on the intercalant-doped $C_{60}$ compounds to examine charge transfer effects.[34]

## 2.1.2 Transport Measurements

In 1991, it was reported that alkali metals intercalated into crystalline $C_{60}$ would cause the $C_{60}$—ordinarily a semiconductor with a gap of ~2.46 eV[35-38]—to conduct.[23] It was soon discovered that $A_x C_{60}$ (A = Alkali metal) passed a resistivity minimum at x = 3, with x = 0 and x = 6 both forming insulating states. The absolute resistivity at x = 3 depends upon the dopant, ranging from ~1–100 mΩ·cm, in contrast to normal metals with resistivities on the order of μΩ·cm. However, $A'_3 C_{60}$ (A′ = K, Rb, Cs) compounds were found to superconduct at relatively high temperatures (from 18 K to 33 K, for review see reference 39).

For $A_3C_{60}$, it is suspected that superconductivity is mediated by only the intramolecular (or on-ball) phonon modes (though it has been suggested by some[40] that both inter- and intramolecular phonons play a role, but the intramolecular phonons dominate). For interfacial electron doping, then, it may also be possible to create a superconducting system. However, it is also likely that the proximity of the electron-doped monolayer to normal metal may hinder any superconductivity.

## 2.2 Two Dimensional Electron-doped $C_{60}$

Though compound formation is not possible with all metals, the possibility of interfacial 'compounds' still exists, in which case $C_{60}$ forms a local compound with the metal through the transfer or sharing of charge from a metal surface atom. The physics at this interface is of great interest and there is extensive literature on the subject.[5, 8, 10-13, 41-45] The 2D conducting monolayer that results from charge transfer is the focus of Chapter 5 of this dissertation. There is a third system that involves electron-doped $C_{60}$, which is $C_{60}$:M—$C_{60}$ in a composite with a metal. Although, in general, a given metal will not diffuse into $C_{60}$ interstitial sites, but collect into islands of metal surrounded by $C_{60}$,[46-48] the layers of $C_{60}$ in contact with these metal islands may be electron-doped. This composite system is the focus of Chapter 6.

The introduction of adsorbates onto the surface of a metal film increases the resistance of the film. Before adsorbates collect on the surface, the scattering of conduction electrons from the surface is specular, with the degree of specularity depending on the number of defects in the surface. For an ideal surface, with no defects or step edges, scattering is perfectly specular (Figure 2.3). The introduction of adsorbates on the surface increases the diffusivity of the surface scattering by perturbing the surface

Specular scattering before
introduction of adsorbate
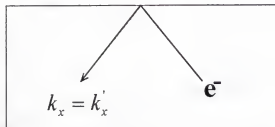
Diffuse scattering after
introduction of adsorbate



$$k_x = k_x'$$  e⁻

$$k_x \neq k_x'$$  e⁻
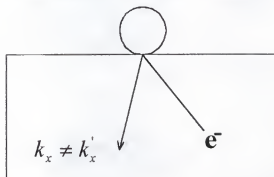
Figure 2.3    Change in scattering from specular to diffuse after the introduction of
adsorbates. The enhancement of surface backscattering increases the
metal's resistance.

potential.[49] The increase in diffuse surface scattering decreases the net forward

momentum of the conduction electrons, thus increasing the resistance of the film. It is

interesting to note that the increase in resistance due to the addition of adsorbates always

occurs for any adsorbate, including metals.[50]

Using a Fuchs-Sondheimer-like model, an expression for the film's resistivity, $\rho$,

can be written.[49]

$$\rho = \rho_0 \left(1 + \alpha \frac{l_0}{d}\right), \tag{2.1}$$

where $\alpha$ is the scattering parameter describing diffusivity, $l_0$ is the mean free path of

conduction electrons, and $d$ is the thickness of the underlayer film. When working with

thin films, it is also useful to define the sheet resistance, $R_{\square}$, of a material. $R_{\square}$ is a

fundamental property of a film that is related to the resistivity. Resistance is defined as

$$R = \frac{\rho\, l}{d\, w}, \tag{2.2}$$

where $l$ is the length of the conduction path, and $w$ the width. The number of squares in the conduction path is $l\,/\,w$, so the resistance per square, or sheet resistance, is

$$R_\square = \frac{\rho}{d}, \tag{2.3}$$

with units $\Omega/\square$. From (2.1) the sheet resistance is then given by

$$R_\square \equiv \frac{\rho}{d} = \frac{\rho_0}{d}\left(1 + \alpha\,\frac{l_0}{d}\right). \tag{2.4}$$

For increases in resistance due only to changes in scattering,

$$\delta R_\square = \frac{\rho_0 l_0}{d^2}\,\delta\alpha\,. \tag{2.5}$$

Some adsorbates may interact with the metal surface such that charge is transferred to or shared with the adsorbate (Figure 2.4). The strength and type of interaction depends on the adsorbate as well as the metal. For instance, metals with lower work functions may donate more charge than those with higher work functions. The removal of charge from the metal causes an increase in resistance, due to depletion of the carrier density. Because of screening effects over a length $\Lambda$, only a small layer of metal near the surface interacts with the adsorbates. Similar to sheet resistance, the sheet conductance of a film of thickness $d$ is given by $G_\square = \sigma d$, which can be rewritten to include the $\Lambda$ correction.

$$G_\square = \sigma(d - \Lambda) + \sigma\Lambda\,. \tag{2.6}$$

Since $\sigma = \frac{ne^2 l_0}{m v_F}$ and $v_F \propto n^{1/3}$, a change in carrier density implies
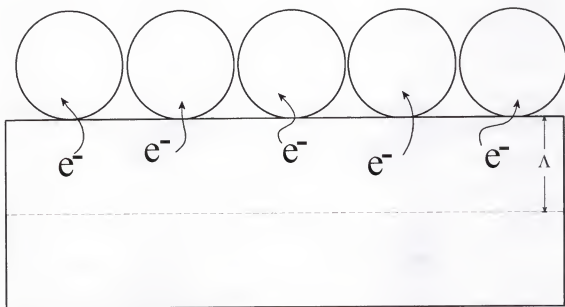
Figure 2.4    Charge transfer to an adsorbate resulting in charge carrier depletion of the underlayer.

$$\frac{\delta\sigma}{\sigma} = \frac{2}{3}\frac{\delta n}{n}.$$ (2.7)

Therefore,

$$\delta G_{\square} = \frac{2}{3}\sigma\Lambda\frac{\delta n}{n}.$$ (2.8)

Since $R_{\square} = \frac{1}{G_{\square}}$,

$$\frac{\delta R_{\square}}{R_{\square}} = -\frac{\delta G_{\square}}{G_{\square}} = -\frac{2}{3}\frac{\delta N_e}{nd},$$ (2.9)

where $\delta N_e = \delta n \cdot d$ is the change in areal density of carriers.

$C_{60}$ is one adsorbate into which charge is transferred from the metal. Typically 1–4 electrons are transferred to each $C_{60}$. For a close packed monolayer of $C_{60}$ with an areal density of $1.11\times10^{14}$ cm$^{-2}$, that corresponds to a $\delta N_e$ of $1$–$4\times10^{14}$ cm$^{-2}$. A typical carrier

density for a metal is ~$10^{23}$ cm$^{-3}$. For a 100 Å film, this corresponds to $N_e = 1 \times 10^{17}$ cm$^{-2}$.

Clearly a change of ~$10^{14}$ cm$^{-2}$ will be negligible for such a film. However, Figure 2.5

shows the resistance increase of a conducting InO$_x$ film after a monolayer of C$_{60}$ is

deposited. This resistance increase is consistent with the removal of charge from an

already small carrier density—on the order of $10^{20}$ cm$^{-3}$—as well as an increase in

scattering. The subsequent decrease in resistance is explained below.



**Resistance versus Time During Deposition of C$_{60}$ on InO$_x$**
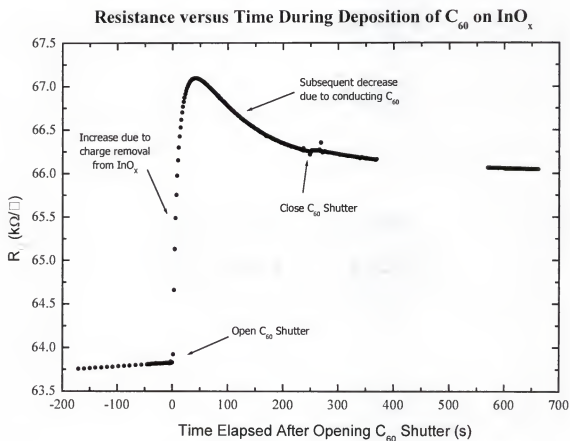
Figure 2.5    Increase in resistance due to diffuse scattering and carrier depletion. Resistance as a function of time during the deposition of C$_{60}$ onto an underlayer of indium oxide. The initial rise in resistance is due to charge depletion in the indium oxide and increased scattering due to the presence of the C$_{60}$ adsorbate. The subsequent decrease in resistance is attributed to the conducting monolayer of C$_{60}$.

An intriguing phenomenon that has been observed for $C_{60}$/M bilayers[2] is the delocalization of the charge acquired from the metal among the $C_{60}$ molecules (Figure 2.6). This delocalization is not typical of all adsorbates, and is usually only seen when the adsorbate is itself a metal. In this case, the $C_{60}$ overlayer forms a parallel conduction path that lowers the total resistance of the bilayer film. For example, Figure 2.7 shows the change in resistance as $C_{60}$ is deposited on a nickel underlayer.

If $R^M$ is the sheet resistance of the metal before $C_{60}$ deposition, and

$$R^B = \left( \frac{1}{R^M} + \frac{1}{R^{C_{60}}} \right)^{-1} \tag{2.10}$$

is the sheet resistance of the bilayer film, then the change in resistance is given by

$$\delta R = \frac{-R^M}{1 + \frac{R^{C_{60}}}{R^M}}. \tag{2.11}$$
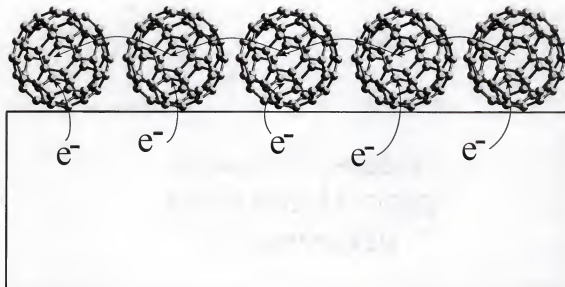


Figure 2.6    Delocalization of transferred charge among a monolayer of $C_{60}$. The addition of a parallel conductor to the system causes a decrease in resistance.

By simply measuring this change in sheet resistance, we can calculate the corresponding sheet resistance of $C_{60}$ needed to cause such a change,

$$R^{C_{60}} = \frac{R^M R^B}{R^M - R^B} \, . \tag{2.12}$$

### 2.2.1 Spectroscopic Measurements

An obvious question that arises is how do we know charge is being transferred to the $C_{60}$ and not *from* the $C_{60}$, enhancing the metal's carrier density? Recall from section 2.1.1 that the $A_g(2)$ vibrational mode shifts approximately 6 cm$^{-1}$ for each electron transferred in bulk $A_3C_{60}$. Similar shifts in the Raman spectra of $C_{60}$ are expected. Chase



**Resistance Decrease From Deposition
of Parallel Conducting C$_{60}$ Monolayer**
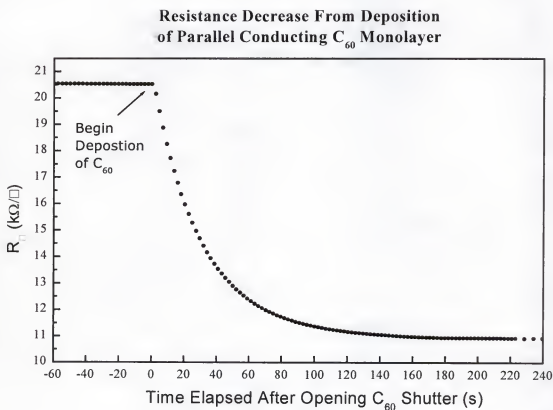
Figure 2.7      Resistance decrease of $C_{60}$/Ni system during deposition of $C_{60}$. The monolayer covering the surface of the nickel becomes conducting, providing a parallel conduction path which decreases the resistance.

*et al*. report such shifts for $C_{60}$/(Au, Cu, Ag), indicating a small charge transfer (~2–4 electrons/$C_{60}$) may be possible.[45] Other methods, such as photoemission,[5, 7, 9, 10, 12, 51] photo-absorption/transmission,[9, 10, 13] high-resolution electron energy loss spectroscopy,[5, 6, 52] and low voltage STM imaging[53] have also indicated charge transfer from the metal to $C_{60}$.

## 2.2.2 Transport Measurements

To date, little work has been done to study the transport properties of the $C_{60}$/M system. The air sensitivity of the samples has limited any such work to *in-situ* growth measurements, similar to those presented here. The first work published on the $C_{60}$/(non-alkali metal) system was in 1992 when Zhao *et al*. presented *in-situ* measurements of $C_{60}$ on tin, barium, gallium, silver, and indium.[54, 55] Their work showed definite, but small decreases in resistance upon the deposition of $C_{60}$ onto the surface of these metals. Their work may have been hindered by poor vacuum conditions (~$2\times10^{-6}$ Torr) which they were able to correct two years later with work published in two papers on samples of $C_{60}$ on copper, chromium, silver, and tin;[43] and copper, chromium, molybdenum, silver, niobium, and titanium,[42] grown in UHV conditions (~$1\times10^{-9}$ Torr). Again, they saw significant decreases in resistance as the $C_{60}$ was deposited and were even able to measure resistance versus temperature for four samples of $C_{60}$/Cu and $C_{60}$/Ag from room temperature to ~100 K. Using a model of two parallel resistors, where one resistor is the underlying metal and the other a metallic interfacial layer, they were able to estimate a resistivity for an electron-doped $C_{60}$ monolayer on copper of ~2000 $\mu\Omega\cdot$cm.

There have been two, more recent papers concentrating on the systems $Cu/C_{60}$ and $C_{60}/Cu$ (Hebard et al.[2]), and $Nb/C_{60}$ and $C_{60}/Nb$ (Wu et al.[46]). Wu et al. showed a resistance decrease for $C_{60}/Nb$, but carried the experiment no further, as they were mainly interested in the percolating systems of $Nb/C_{60}$ and $Nb/C_{70}$. However, Hebard et al. obtained samples of electron-doped $C_{60}$ with resistivities on the order of 800 $\mu\Omega\cdot cm$. A goal of this research was to reproduce these low resistivity electron-doped monolayers and perform transport measurements at temperatures down to 2 K and in bipolar magnetic fields ranging up to 7 T. To achieve this goal, a special UHV vacuum-chamber/cryostat system was constructed. This system, nicknamed SHIVA, will be discussed in Chapter 4.

CHAPTER 3
MAGNETOTRANSPORT IN THIN FILMS

There are numerous texts and papers covering the subject of magnetotransport (or galvanomagnetic) effects[56-62] in metals. A brief description of the effects relevant to this dissertation will be addressed below. Section 3.1 covers magnetoresistance effects and Section 3.2 covers the normal and anomalous Hall effects.

### 3.1 Magnetoresistance

In general, the application of a magnetic field changes the resistance of a material. This magnetoresistance is usually discussed as the ratio,

$$\frac{\Delta R}{R} = \frac{R(H) - R(0)}{R(0)}, \tag{3.1}$$

of the difference between in-field and zero-field resistance with the zero-field resistance. Magnetoresistance can also be thought of as a derivative, $\frac{\partial R}{\partial H}$, since the local slope of the resistance versus field curve may change in different field regimes. There are two kinds of magnetoresistance—longitudinal and transverse.[62] When $\vec{H}$ is parallel to $\vec{J}$ and voltage is measured between points A and B (Figure 3.1a), the magnetoresistance is called longitudinal magnetoresistance. When $\vec{H}$ is perpendicular to $\vec{J}$ and voltage is measured between A and B (Figure 3.1b), it is called transverse magnetoresistance. A
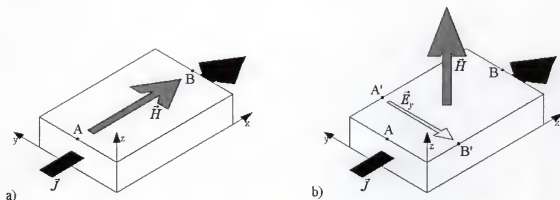
Figure 3.1    Field and current orientation for magnetotransport measurements.
a) The longitudinal orientation.  Longitudinal magnetoresistance is
calculated from $V_{AB}$ divided by the current, $I = J \cdot d \cdot w$, where $d$, and $w$
are the thickness and width of the sample.  b) The transverse
orientation.  Transverse magnetoresistance is calculated from $V_{AB}$
divided by $I$; Hall resistivity is calculated from $V_{A'B'}$ times $d$ divided by

measurement of magnetoresistance with $\vec{H}$ perpendicular to $\vec{J}$ but *in the plane of the*

*sample* (not shown) also called transverse magnetoresistance.

When $\vec{H}$ is at some arbitrary angle with respect to $\vec{J}$, the magnetoresistance is a

mixture of longitudinal and transverse magnetoresistance.  Formally, from Ohm's law in

tensor form,

$$\vec{E} = \boldsymbol{\rho} \cdot \vec{J}, \tag{3.2}$$

where $\vec{E}$ is the electric field needed to produce $\vec{J}$, and $\boldsymbol{\rho}$ is the resistivity tensor.  For an

arbitrary alignment of fields,

$$\boldsymbol{\rho} = \begin{bmatrix} \rho_{xx} & \rho_{xy} & \rho_{xz} \\ \rho_{yx} & \rho_{yy} & \rho_{yz} \\ \rho_{zx} & \rho_{zy} & \rho_{zz} \end{bmatrix}. \tag{3.3}$$

When the fields are aligned in the longitudinal orientation (Figure 3.1a), $\rho_{ll} = \rho$,

and $\rho_{ij} = 0$, $i \neq j$, as all fields and currents point in the x-direction. For the transverse

orientation (Figure 3.1b), $\rho_{ii}$ is again simply $\rho$ to first order, but $\rho_{ij} \neq 0$ for all $ij$. This

phenomenon is called the Hall effect and will be addressed in Section 3.2. There are

many factors that affect the MR of a material, such as the shape of the Fermi surface, and

the kinds of scattering the electrons undergo.

In general, at low fields ($\omega_c \tau << 1$, where $\omega_c$ is the cyclotron frequency and $\tau$ is

the mean electron scattering time), the magnetoresistance is positive and quadratic in $\vec{H}$.

At higher fields, the dependence can be quite different. For crystalline samples, the

transverse magnetoresistance is largely dependent on the shape of the Fermi surface.

When a magnetic field is applied to a metal, the Lorentz force causes the electrons to

orbit around the field lines with frequency $\omega_c = eH/m^*$, where $m^*$ is the effective mass

of the electrons and $e$ the electric charge. In momentum-space, the orbits must follow

the Fermi surface. If the orbit encloses a region where all states are of lower energy, it is

electron-like; if it encloses a region of unfilled, higher energy states, it is hole-like. If the

orbit is confined inside the Brillouin zone, it is said to be closed. Electrons in closed

momentum- space orbits are forced by $\vec{H}$ to undergo periodic, real-space motion in the

direction of $\vec{J}$ (Figure 3.2). If, however, the orbit is oriented such that it passes along a

neck of the Fermi surface into the next zone and so on through every zone ad infinitum, it

is an open orbit. Electrons in open orbits are not constrained to periodic real-space

motion, as for closed orbits. For a more detailed discussion of open and closed orbits

with illuminating figures, see Ashcroft and Mermin[63] or Pippard.[56] Depending on the

orientation of $\vec{H}$ with respect to the crystal axes, the electrons can have either open or
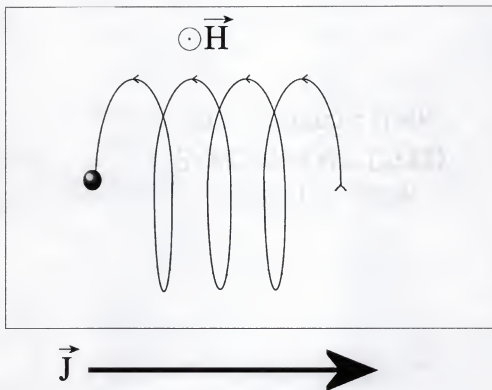
Figure 3.2    Real-space motion of a conduction electron in a closed momentum-space orbit in the presence of a magnetic field.

closed orbits, or both. If only closed orbits are possible, then at high fields ($\omega_c \tau \gg 1$) the magnetoresistance will saturate. If open orbits are possible, then the magnetoresistance will continue to rise quadratically in $\vec{H}$.

For magnetic materials, the transverse magnetoresistance is usually negative. At zero $\vec{H}$, the magnetic moments in the material are randomly oriented. The conduction electrons scatter off the magnetic moments in the material, with the electron spins also oriented randomly with respect to the magnetic moments. The randomness in the magnetic moments is seen by the electrons as an aperiodic potential which inhibits the formation of Bloch waves. The application of a magnetic field tends to align the
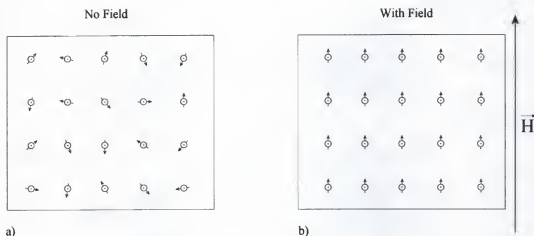
Figure 3.3    Saturation of magnetic moments.  a) Without an external field, the
              magnetic moment domains are randomly oriented.  Because of this
              randomness, the conduction electrons see an aperiodic potential, which
              disrupts their Bloch wave nature, increasing resistance.  b) Application
              of an external magnetic field aligns the magnetic moments, restoring
              the periodic potential and reducing the resistance of the sample.

magnetic moments with each other (Figure 3.3) and the electron spins with the magnetic

moments.  The alignment of the magnetic moments reduces the disorder of the system,

hence reducing the magnitude of the scattering and decreasing the resistance.  As $\vec{H}$ is

increased, and the sample magnetization saturates, the negative magnetoresistance

saturates.  For clean systems, after this saturation, the magnetoresistance should return to

the quadratic-in-$\vec{H}$ behavior described above for a general material.

The longitudinal magnetoresistance in magnetic materials tends to be positive at

low fields.  This difference in sign of the magnetoresistance for the two orientations is

called anisotropic magnetoresistance, and can be attributed to a difference in the spin-

orbit coupling of the conduction electrons for the two orientations.[64, 65]  After saturation

of the sample magnetization, the magnetoresistance returns to the $H^2$ form and has

qualitatively the same shape as the transverse magnetoresistance. Because orbital effects will be stronger in the transverse direction, the after-saturation magnetoresistance will typically be quantitatively different for the two orientations.

For disordered materials, the magnetoresistance can also be negative due to an effect called weak localization.[66-68] The theory of weak localization describes the deviation from classical resistance of a material when the quantum mechanical wave nature of the electrons is considered. Due to the scattering of conduction electrons around closed paths, the wavefunctions of the electrons interfere in such a way that there is an increased probability of the electron remaining at the origin of a given scattering path (Figure 3.4). This localization of the electron manifests itself as an increase in resistance.

The cutoff length scale, $L_\phi$, describes the average distance an electron will travel before it experiences an event that erases its phase information. Such events can be electron-phonon or electron-electron interactions.

$$L_\phi = \sqrt{D\tau_\phi} \tag{3.4}$$

where $D$ is the electron diffusion constant and $\tau_\phi$ is the average time between phase-breaking events, which is proportional to temperature raised to a power, $P$. The sheet conductance is related to $\tau_\phi$ by the following equation:[66]

$$\frac{\Delta G}{G_{00}} = \ln\left(\frac{\tau_\phi}{\tau_0}\right) = p\ln(T); \quad \tau_\phi \propto T^{-P}; \quad G_{00} = \frac{e^2}{2\pi^2\hbar}. \tag{3.5}$$

$\Delta G$ is the sheet conductance of the sample minus the classical sheet conductance, and $p = \alpha P$, where $\alpha$ depends on the strengths of spin-orbit and magnetic scattering, and $P$
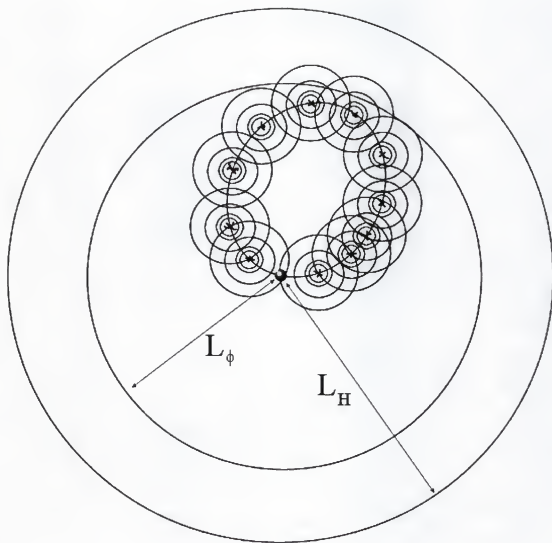
Figure 3.4    Schematic of the interference of scattered electron wavefunctions. The electron (represented by the ball at the center of the picture) can scatter around a closed path in two possible directions. Quantum mechanically both paths are sampled. From each scattering site emanates a new wavefront that interferes with all other wavefronts. The interference produces an enhanced probability of the electron remaining at the origin of the scattering path.

depends on the dephasing mechanism for the electrons.[69] Therefore, in a sample showing weak localization, a plot of its sheet conductance versus log(T) should be a straight line, with slope proportional to $p$.

From magnetoresistance measurements of the sample, $\tau_\phi$ can be obtained. Upon application of a magnetic field, the weak localization is suppressed, and the resistance decreases. The magnetoresistance has the form of the digamma function, $\Psi$:[70, 71]

$$\frac{\Delta G}{G_{00}} = \alpha \left[ \Psi\left(\frac{1}{2} + \frac{H_\phi}{H}\right) - \ln\left(\frac{H_\phi}{H}\right) \right], \qquad (3.6)$$

where $H_\phi = \dfrac{\hbar}{4eD\tau_\phi}$, $D = \left(e^2 N R_{\square} d\right)^{-1}$, and N is the density of states. Therefore, from

measurements of the magnetoresistance one can obtain a value for $L_\phi = \sqrt{\dfrac{\hbar}{4eH_\phi}}$, using

$H_\phi$ as a fitting parameter for Equation 3.6. If the density of states is known for the material, then $\tau_\phi$ can also be calculated from $H_\phi$. Independent measurements of $G$ versus temperature and magnetic field can determine $\alpha$ and $P$.

### 3.2   Hall Effect

In the transverse field orientation (Figure 3.1b), the Lorentz force tends to force the electrons, or holes, to the negative-y side of the sample, where they build up until the repulsive force balances the Lorentz force. When magnetic field is added, equation (3.1) becomes

$$\vec{E} = \rho\vec{J} + R_0(\vec{H} \times \vec{J}). \qquad (3.7)$$

As equilibrium between the Lorentz and Coulomb forces develops, a transverse electric field,

$$\vec{E}_y = R_0(\vec{H} \times \vec{J}), \tag{3.8}$$

develops perpendicular to $\vec{J}$ and $\vec{H}$. In this case the off diagonal elements from (3.2) are

$$\rho_{xy} = -\rho_{yx} = \rho_H = R_0 H, \tag{3.9}$$

where $R_0 = 1/ne$, is the Hall coefficient and $n$ is the carrier density of the material. All other off-diagonal elements of $\boldsymbol{\rho}$ are zero. From measurements of the Hall resistivity, $\rho_H$, as a function of $\vec{H}$, $n$ can be calculated (Figure 3.3). Also, from the Drude model of conductivity,

$$\rho^{-1} = ne\mu, \tag{3.10}$$

where $\mu$ is the carrier mobility. Using the Hall measurements to provide $n$, a measurement of $\rho$ at zero $\vec{H}$ can be used to calculate $\mu$. From these two simple measurements, a basic understanding of the electronic behavior of the system can be achieved.

For magnetic materials, the intrinsic magnetization also plays a roll in the Hall effect. Equation 3.6 becomes

$$\vec{E} = \rho\vec{J} + R_0(\vec{B} \times \vec{J}); \quad \vec{B} = \vec{H} + \vec{M}. \tag{3.11}$$

The Hall resistivity is then given empirically by[57, 72]

$$\rho_H = R_0 B + R_1(M + \frac{\partial M_S}{\partial H} B). \tag{3.12}$$

Substituting in $\vec{B}$ and collecting terms in $H$ and $M$,

$$\rho_H = (R_0 + R_1 \frac{\partial M_S}{\partial H})H + R_S M \ . \tag{3.13}$$

$$R_S = R_1(1 - \frac{\partial M_S}{\partial H}) - R_0 \tag{3.14}$$

is called the spontaneous, or anomalous Hall coefficient, and $R_1 \frac{\partial M_S}{\partial H}$ is the forced[72]

Hall coefficient. Typical treatments of the Hall effect in ferromagnets ignore the forced

Hall coefficient, as it is usually smaller than $R_0$ for low temperatures. For nickel, at least,
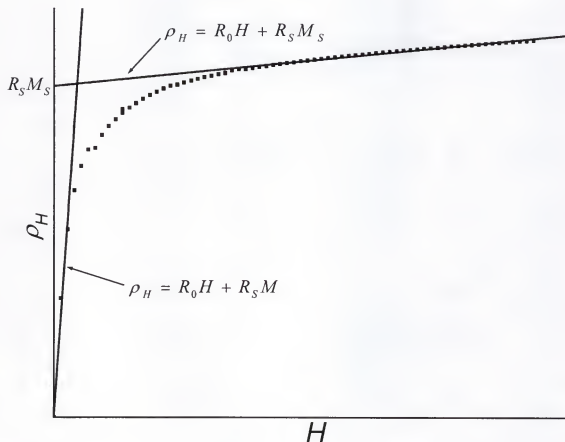


Figure 3.5    The anomalous Hall effect as seen in a thin nickel film. The initial
steep slope is caused by the presence of the ferromagnet's
magnetization. After $M_S$ is reached, the resistivity change returns to the
normal Hall effect slope. In general, both $R_S$ and $M$ are functions of $H$.

it has been shown that the forced Hall coefficient is negligible compared to $R_0$, even up to room temperature.[73] Hence, for the purposes of this dissertation, $R_1 \dfrac{\partial M_S}{\partial H}$ will be dropped and

$$\rho_H = R_0 H + R_s M \ . \tag{3.15}$$

The effect of the magnetization term in Equation 3.15 is to cause a deviation from the normal linearity of the Hall effect at low fields ($H < H_{saturation}$) (Figure 3.5). Once the saturation magnetization, $M_S$, is reached, the Hall effect returns to its normal linear dependence on $\vec{H}$, and $R_0$ can again be calculated from the slope of the curve. In addition, the intercept of the fit above the saturation field gives a measure of the magnetization of the sample.

CHAPTER 4
EXPERIMENTAL DETAILS

This chapter focuses on the experimental setup for sample fabrication, and characterization of the $C_{60}$/M bilayer and $C_{60}$:$Ni_x$ composite films. The two vacuum systems used to grow the samples will be examined, and the equipment and techniques used for *in situ* and *ex situ* measurements of the film characteristics will be described.

### 4.1 *In Situ* Growth Measurements on $C_{60}$/M and $C_{60}$:$Ni_x$

Two vacuum systems were used in the completion of this research—one high vacuum, and the other near ultra-high vacuum ($10^{-9}$–$10^{-12}$ Torr). The high vacuum chamber, nicknamed Oz, uses a diffusion pump with a liquid nitrogen cold trap, and typically obtains a base pressure of $4 \times 10^{-8}$ Torr. Although this pressure is sufficient for our applications, the system is inherently dirty, due to the oil vapors from the diffusion pump. Since we are working with a system of carbon molecules, we may be sensitive to contamination by pump-oil hydrocarbons.

In Oz, where the $C_{60}$/Ni films were grown, deposition was performed using an Omicron EF3 three-source electron bombardment deposition system. A very compact system fitted on a two and three-quarter inch conflat flange, the Omicron uses electron bombardment to heat sources to the evaporation/sublimation point. Efflux from the source then condenses on the substrate. Some efflux becomes ionized as it passes

through the oncoming cloud of electrons from the filament source. These ions are detected by a Faraday cup, allowing for measurement of a current proportional to the mass flux from the source. Thickness calibrations must be performed for each new filament, as line-of-sight current leakage from the filament to the Faraday cup changes from filament to filament.

The omicron houses three sources, which can be either wires or crucibles, and deposition from each source can be achieved simultaneously or sequentially, using a rotatable shutter that allows for any combination of sources to be exposed to the substrate. The efflux from the three sources impinges upon an area of approximately two centimeters in diameter, with uniform spot coverage and good overlap of coverage area. Consequently, a shadow mask can be used to delineate the films without significant mismatch of layers due to source geometry (Figure 4.1).

To allow the growth and measurement of air sensitive samples, a second chamber, nicknamed SHIVA (for Sample Handling In Vacuum), was built. SHIVA uses an oil-
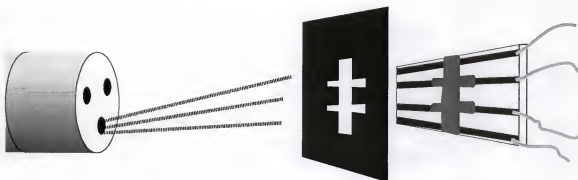


Figure 4.1    Schematic of sample deposition from Omicron EF3 source through a shadow mask onto a glass substrate. Not shown is the rotatable shutter that allows various combinations of sources to be exposed to the sample. Due to the displacement of the three sources, there is a very small mismatch of the three shadows.

less, or dry, roughing pump in conjunction with a cryopump, and typically reaches a base pressure of $2 \times 10^{-9}$ Torr. Since a cryopump works by freezing out any gases, the chamber will remain free of hydrocarbons as long as they are not introduced with samples. The biggest success of SHIVA is the load lock system, which allows the movement of samples into and out of the chamber without venting. Not having to vent the chamber to load and unload samples permits the ultra-high vacuum region to be achieved by pumping for long periods, while maintaining the flexibility of inserting and removing samples on a daily basis. The SHIVA vacuum system was designed to allow for *in situ* growth measurements, followed by transfer of the sample into a UHV cryostat (the ShivaStat), without breaking vacuum. RGA analysis of the background pressure in SHIVA indicates it is due mostly to water, with trace amounts of $H_2$, He, $N_2$, $O_2$, CO, and $CO_2$. The deposition chamber is fitted with several sources. Two magnetron sputter guns and two Radak resistively-heated crucibles are permanently mounted, while the Omicron source can be moved between Oz and SHIVA.

In both systems, vacuum electrical feedthroughs allow for four-terminal resistance measurements during sample growth. The bilayer samples were grown in two stages. First, the metal underlayer was grown through a shadow mask on a pre-cleaned,[*] microscope-slide-glass substrate with pre-deposited Au/Cr electrical leads. Then the $C_{60}$ was deposited on top of the metal film through the same mask without breaking vacuum. The composite samples were grown in the same manner, except the $C_{60}$ and nickel were co-deposited. All data acquisition was controlled by LabVIEW Virtual Instruments

---

[*] The method of substrate cleaning is as follows: Ultrasonication at 45° C first in detergent and deionized water for 60 minutes, then 15 minutes each of deionized water, acetone, isopropanol, then methanol. The substrates are then blown dry with filtered, dry, nitrogen gas, and stored in a desicator.

(VI's). The following two sections describe in more detail the measurements performed in each system.

### 4.1.1  Growth of $C_{60}$/Ni and $C_{60}$/Cu Bilayers

Resistance measurements of the nickel underlayer of the $C_{60}$/Ni films, grown in Oz, were performed during deposition with a Keithley Instruments model 236 Source Measurement Unit in voltage source mode. Sample resistance and source efflux were monitored as a function of time. The source voltage was set alternately at ±1 mV, the current read, and the readings subtracted, to extract any current offset due to ions impinging on the sample. Deposition was stopped at pre-selected target resistances. The geometry of the shadow mask used in the Oz system was such that the distance between voltage leads was twice the width of the sample. Hence, $R_{\square}$ was simply half the total resistance.

For the $C_{60}$ deposition, resistance was monitored with a Linear Research LR-700 Resistance Bridge, which makes a 17 Hz, four-terminal, constant current measurement. The minimum time between deposition of the nickel and deposition of the $C_{60}$ was limited only by how rapidly the $C_{60}$ crucible could be brought to operating temperature. A sticky spot in the rotation of the shutter on the Omicron made it difficult to effectively shutter the $C_{60}$ source while depositing the nickel. Therefore, the $C_{60}$ source was kept cold during the nickel evaporation; however, the $C_{60}$ was degassed up to deposition temperature prior to the nickel deposition. A typical post-nickel deposition warm-up time for the $C_{60}$ crucible was ~5 minutes.

In anticipation of using the ShivaStat for transport measurements on these air sensitive films, the $C_{60}$/Cu samples were grown in SHIVA. Unlike the $C_{60}$/Ni system,

resistance measurements during copper film deposition could not be performed with the Keithley 236, since a sputter gun was used for the deposition. Because the dc leakage current from the dc sputter gun to the sample was on the order of the model 236 measurement-current-limit (~10 μA), a Princeton Applied Research PAR124A or a Stanford Research SR830 lock-in amplifier, operating at 17 Hz, was used for resistance measurement instead. A ballast resistor of ~1MΩ was used to limit the current to ~1μA. The same setup was used again for the measurement of resistance during the $C_{60}$ deposition.

### 4.1.2 Growth of $C_{60}$:$Ni_x$ Composites

Two of the $C_{60}$:$Ni_x$ samples and the pure nickel film were grown in Oz. The deposition setup was the same as for the $C_{60}$/Ni samples described in section 4.1.1, except the Omicron was used to co-deposit nickel and $C_{60}$, instead of depositing them sequentially. Again, the Keithley 236 Source measurement unit was used to measure resistance during deposition. The samples were then removed for *ex situ* transport measurements, as described below in section 4.2.2.

For the $C_{60}$:$Ni_x$ sample grown in SHIVA, the Omicron EF3 was again used. The SHIVA sample stage is rotatable, so the plane of the sample can be made normal to each source. Hence, a shadow mask was used to delineate the films, as for growth in the Oz system. Substrates were prepared as described in the previous section. Thicknesses were monitored with a quartz crystal oscillator controlled by an Inficon IC5 crystal monitor.

Due to the nature of the $C_{60}$/M experiments, only the resistance of the metal underlayer was of consequence. Hence, little attention was paid to the actual thicknesses

of the underlayers. However, for the composite system, it was necessary to know the ratio of $C_{60}$ to nickel. Though Oz was equipped with a crystal thickness monitor, it could not be positioned close enough to the sample to be used. Therefore, for the experiments with $C_{60}:Ni_x$ composites, the Omicron source was moved to SHIVA. The sample stage in SHIVA can be moved back and forth and rotated to position the face of the crystal thickness monitor normal to the source. Before and after the composite deposition in SHIVA, the deposition rates for $C_{60}$ and nickel were measured, and the $C_{60}:Ni_x$ ratios were subsequently determined. A calibration run to determine the ratios of $C_{60}:Ni_x$ films grown in Oz was also performed. Measurements of the flux and thickness rate, as measured by the IC5 thickness monitor, were taken at the deposition parameters used for the Oz growths. From this calibration, and knowledge of the average fluxes during Oz deposition, stoichiometries were calculated with reasonable error bars.

Being a crucible of considerable mass, the $C_{60}$ source had a large thermal time constant, so the $C_{60}$ mass flux remained nearly constant for the duration of deposition. However, the wire nickel source's efflux depended greatly on the proximity of the tip to the electron filament. During the deposition, enough mass was ejected from the source to decrease the proximity of the source tip to the filament, thus decreasing the efflux. Although the EF3's power supply has a feedback loop to keep the flux roughly constant, it was not capable of compensating for the decreasing length of the nickel wire. To counteract the decreasing flux trend, the wire was manually fed closer to the electron filament as needed to stabilize the nickel flux.

## 4.2 Transport Measurements

Electronic transport and magnetotransport measurements were made in two cryostat systems. For samples made in SHIVA, the ShivaStat was used. For the $C_{60}$:$Ni_x$ samples made in Oz, a Quantum Design Physical Properties Measurement System (PPMS) was used. The ShivaStat was designed and built in-house specifically for making standard cryostat measurements in a UHV environment. Using the ShivaStat, air sensitive samples, like the $C_{60}$/M samples, could be subjected to low temperatures (~2 K) and high magnetic fields (~7 T), without being exposed to air. The $C_{60}$:$Ni_x$ samples turned out to be mostly air insensitive, showing only minimal resistance changes due to room temperature air exposure. Hence, a commercial, automated cryostat was used for magnetotransport measurements on the composite films, but the $C_{60}$/M samples required the use of the ShivaStat.

### 4.2.1 ShivaStat

A $C_{60}$/Cu sample was loaded into the ShivaStat for transport measurements. Resistance as a function of temperature was measured from 2–250 K, and magnetoresistance was measured up to 7 T using a PAR124A lock-in amplifier operating at ~17.7 Hz. The same 1 MΩ ballast resistor mentioned in section 4.1.1 was again used to limit current to ~1μA. The magnet was controlled using an American Magnetics 4Q-01500 four-quadrant magnet power supply and AM420 power supply controller. The temperature was determined by measurement of the resistance of a cernox thermometer clamped to the same copper sample holder upon which the sample was mounted. The temperature was calculated by interpolation of a lookup table generated by calibration of the thermometer in the PPMS system described below.

### 4.2.2 Physical Properties Measurement System (PPMS)

The PPMS is capable of making ac or dc measurements on samples at temperatures ranging from 2–300 K, and in bipolar magnetic fields of up to 7 T. In addition to the standard PPMS system, a special horizontal rotator insert is used, which allows the PPMS to control the angle of the sample surface with respect to the magnetic field. The PPMS can be automated by using sequence files downloaded to its CPU, or by using LabVIEW VI's and a GPIB interface. The data for the $C_{60}:Ni_x$ samples were taken using LabVIEW and either the LR-700 or a homemade resistance bridge and two PAR 124A lock-in amplifiers, as availability permitted. The LR-700 has better common mode rejection than the ac bridge provided with the PPMS, and some samples had large contact resistances, making the PPMS AC Transport bridge measurements too noisy. The LR-700 has a $10\Delta R$ mode that balances the signal to zero, providing five decimal precision on low level signals. This precision was needed as the magnetoresistance for the composites was on the order of 0.1% or less. The homemade bridge and lock-in setup reproduced this precision as well.

CHAPTER 5
THE $C_{60}$/M BILAYER FILMS

This chapter covers the measurements of resistance during the growth of $C_{60}$

monolayers on underlayers of nickel, and copper.  From these measurements, the sheet

resistance of electron-doped $C_{60}$ on the different substrates is calculated.  Also discussed

are the transport measurements performed on each system.

## 5.1   The $C_{60}$/Ni System

The work done on $C_{60}$/Ni bilayers was completed in the Oz system.  Samples were

grown sequentially, as discussed in Chapter 4.  Fifteen samples were made during this

part of the research.  Of these fifteen, thirteen were used for subsequent $C_{60}$ deposition.

The other two were nickel calibration samples used to optimally set deposition

parameters.  A typical nickel film deposition is shown in Figure 5.1.  Notice that the noise

ceiling for the measurement is around $10^7$ Ω.  In the leftmost region of the data (-175–200

s), the noise is associated with tunneling across the surface of the glass substrate.  The

adsorbates inherent in the Oz system provide hopping states for the conduction electrons.

As the nickel starts to collect on the surface, a region is reached (here, around 200 s)

where the nickel grains are close enough for hopping to occur directly between them.  As

the grains grow, the hopping becomes easier and the resistance decreases.  Eventually a

point is reached (here, around 275 s) where a percolating network of nickel grains forms.

**Nickel Underlayer Deposition**
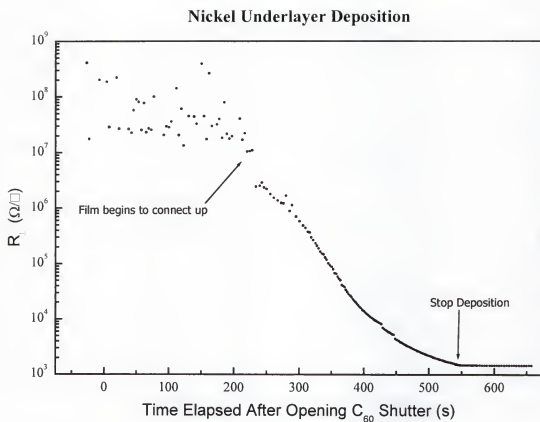
Figure 5.1    Sheet resistance as a function of time elapsed from opening the deposition shutter, during the deposition of a nickel underlayer. The stopping resistance here was ~1200 $\Omega/\square$. The noisy region on the left side of the curve, between zero and 200 seconds, is associated with leakage current across the empty substrate. The nickel film does not start to conduct until around 200 seconds.

From there, continued deposition fills in the holes in the percolating network. Because of the noise ceiling, measurements of the nickel resistance above 1 M$\Omega$ are untrustworthy.

The target sheet resistances of the nickel underlayers were chosen to be in a range of 1–100 k$\Omega/\square$. After a metal film is deposited, thermal excitations drive a period of reconstruction of the film morphology, called room temperature annealing. The film may slowly wet the substrate, or ball up on the substrate, depending on the surface interactions of the material with the substrate. The surface of the film itself may change with time, as

**Room Temperature Post-Deposition Annealing
for a Typical Nickel Film**
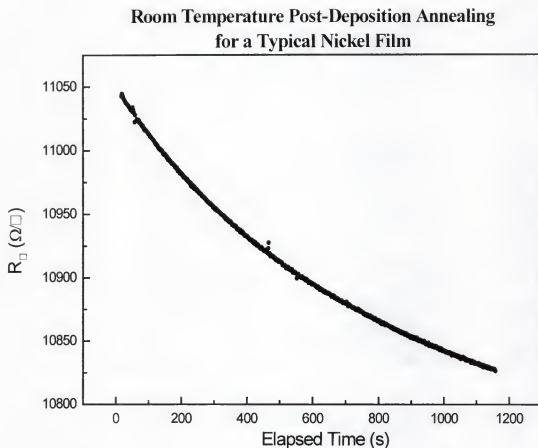


Figure 5.2    Room temperature annealing resistance decrease for a typical film of
nickel.  For stopping resistances of around 250 k$\Omega$ or less, the
resistance is seen to decrease during annealing.  Films with higher stop-
growth resistances will show a resistance increase during annealing.

contaminants in the vacuum system are adsorbed, or as the atoms of the surface rearrange

themselves.  The reconstruction manifests itself as a change in resistance as the film

anneals.  For nickel films with an end-growth resistance of less than 220 k$\Omega/\square$, the

annealing decreases the resistance (Figure 5.2).  Hence, it is difficult to precisely reach a

target resistance, but it is possible to reach within 10% of the target value.

### 5.1.1 Sheet Resistance of $C_{60}$

After the nickel underlayer reaches its target resistance, the deposition is stopped and the $C_{60}$ source is warmed up. The deposition of the $C_{60}$ takes place as soon as a stable flux can be achieved. This typically takes anywhere from 5–15 minutes. It is during this time that the annealing data for the underlayer are taken. Once the $C_{60}$ source is ready, the shutter is opened and the resistance is seen to drop immediately (within the time between data points, approximately 2–3 seconds). The resistance continues to decrease until a physical monolayer (complete coverage by the adsorbate such that there are ideally no holes to the substrate) covers the nickel surface. When $C_{60}$ is deposited on a room temperature substrate, the growth mechanism can vary depending on the substrate. There is evidence that $C_{60}$ deposited on the noble metals and some semiconductor surfaces will form a monolayer first, before building islanded second layers[53, 74-77]. For the deposition of $C_{60}$ on transition metal surfaces, it may form small clusters 2–3 layers thick, before the entire substrate is covered.[41] Therefore, more $C_{60}$ must be deposited than what would be required if the adsorbing molecules formed a monolayer immediately. A typical resistance decrease during $C_{60}$ deposition is shown in Figure 5.3.

For the $C_{60}$/Ni system, a survey of initial nickel resistances ranging from approximately 1–200 k$\Omega$ was performed, the results of which are summarized inFigure 5.4. The figure is divided into three regions to facilitate an explanation of the scatter of the data. From the formalism in section 2.2, the $C_{60}$ sheet resistance ( $R^{C_{60}}$ ) should be independent of the nickel sheet resistance ( $R^{Ni}$ ). The deviations from constant $R^{C_{60}}$ can be explained in two ways, depending on the region of the plot. The right-most region is simplest to explain. Here the nickel underlayer is so thin it is discontinuous.

Conduction still occurs in such an inhomogeneous film, through hopping between

clusters

of nickel, but there are sections of glass uncovered by nickel. Any $C_{60}$ deposited on the

holes in the nickel film will not be doped. As far as conduction is concerned, these

undoped regions are essentially holes in the $C_{60}$ monolayer. Hence, the sheet resistance

**Resistance vs. Time During Deposition of $C_{60}$ on Nickel Underlayer**



$$R_{\square}^{C_{60}} = \frac{R_{\square}^{M} R_{\square}^{B}}{R_{\square}^{M} - R_{\square}^{B}}$$

Open Shutter to $C_{60}$

$\Delta R_{\square} \sim 11\%$
$R_{\square}(C_{60}) \sim 85\ k\Omega/\square$

Close shutter

Time Elapsed After Opening $C_{60}$ Shutter (s)
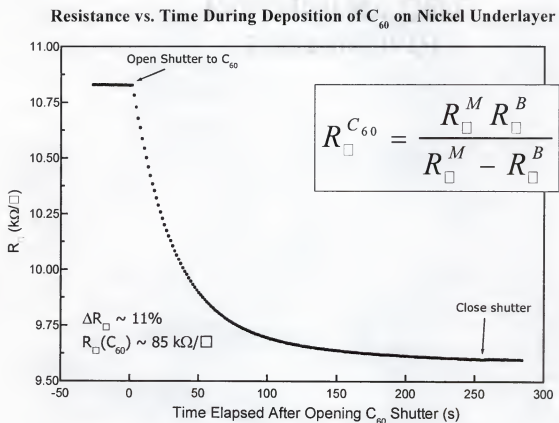
Figure 5.3    Sheet resistance as a function of time during the deposition of $C_{60}$ onto a nickel underlayer. Notice the 11% decrease in resistance between the opening of the shutter to $C_{60}$ and closing it. Approximately 30 Å of $C_{60}$ has been deposited by the close of the shutter. Due to low mobility of $C_{60}$ on nickel, one must deposit enough $C_{60}$ to make up three or four monolayers before a physical monolayer covers the nickel surface. The boxed formula is used to calculate the $C_{60}$ sheet resistance ($R_{\square}^{C_{60}}$).

$R_{\square}^{M}$ is the sheet resistance of the metal before $C_{60}$ deposition. $R_{\square}^{B}$ is the sheet resistance of the bilayer system after $C_{60}$ deposition.

of the entire film is increased, even though small, homogeneous, sections of the bilayer film, if isolated, would have the sheet resistance seen in the flat, middle region of Figure 5.4.

Using only the five data points in the middle region of Figure 5.4, an average yields a sheet resistance of $59000\pm13000$ $\Omega/\square$. Assuming a $C_{60}$ monolayer thickness of approximately 10Å, this sheet resistance corresponds to a $C_{60}$ resistivity of ~6 $m\Omega\cdot cm$.

**Calculated $C_{60}$ Sheet Resistance vs. Nickel Sheet Resistance**
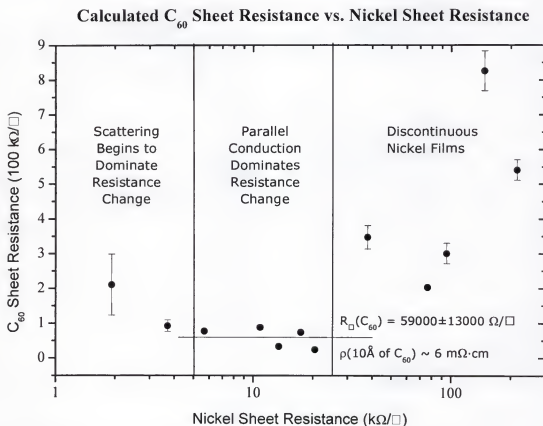


Figure 5.4    Scatter plot of $C_{60}$ sheet resistance versus nickel sheet resistance. The three regions are discussed in depth in the text. The rightmost region shows data for $C_{60}$ on discontinuous nickel films. In the middle, the nickel is continuous and of high enough resistance to show a large decrease when $C_{60}$ is added on top. In the leftmost region, the resistance increase due to added scattering outweighs the resistance decrease from the conducting $C_{60}$.

The variation of the 'flat' region of data can be accounted for by differing nickel annealing times and background pressures. The larger values of $R^{C_{60}}$ are likely caused by adsorbates other than $C_{60}$—like pump-oil vapor, oxygen, nitrogen, etc.—inhibiting the charge transfer from the metal to the $C_{60}$.

It is, in part, the variation in surface quality that provides such a large uncertainty on the average value of $R^{C_{60}}$, compared to the individual uncertainties of the data points. $R^{C_{60}}$ for an individual sample can be calculated fairly accurately, as it depends most strongly on $\Delta R$, which is easily measured for the samples in the middle region of Figure 5.4. But because the resistance of an individual conducting $C_{60}$ monolayer can vary greatly, depending on the underlayer quality, the ideal resistance for electron-doped $C_{60}$ cannot be determined with greater accuracy unless a better method of controlling the metal underlayer surface quality can be developed. The second factor determining the uncertainty in $R^{C_{60}}$ is the irreproducibility of $R^{Ni}$ (or $R^{Cu}$, see section 5.2.1). The post deposition annealing of the underlayer metal makes it difficult to produce the same underlayer resistance twice, much less often enough to provide a statistical basis for the uncertainty in $R^{C_{60}}$.

The left-most region of the plot can be explained as a crossover region. Recall that Equation 2.10 gives the bilayer sheet resistance as a function of $R^{C_{60}}$ and $R^M$. This equation does not take into account the change in the sheet resistance of the underlying metal film due to increased surface scattering or charge carrier depletion. In actuality

$$R^B = \left( \frac{1}{R^{M*}} + \frac{1}{R^{C_{60}}} \right)^{-1}$$

(5.1)

where $R^{M*}$ is the sheet resistance of the metal altered by scattering and charge carrier depletion effects. In this case, Equation 2.12,

$$R^{C_{60}} = \frac{R^M R^B}{R^M - R^B} \qquad (2.12)$$

becomes

$$R^{C_{60}*} = \frac{\left(R^M + \delta R^M\right)R^B}{\Delta R + \delta R^M} \qquad (5.2)$$

where $\delta R^M = R^{M*} - R^M$ and $\Delta R = R^M - R^B$. It is easily seen that when $\delta R^M$ is much less than $R^M$ and $\Delta R$, (5.2) reduces to (2.12). The condition $\delta R^M \ll R^M, \Delta R$ holds true in the right-most and middle regions of Figure 5.4, but not in the left-most region. As $R^M$ decreases, the change in resistance caused by the addition of a parallel resistor of fixed resistance also decreases, leaving $\Delta R \sim \delta R^M$. Because (2.12) is used to calculate $R^{C_{60}}$ (since $\delta R^M$ is unknown), when $\delta R^M$ is not negligible, an erroneously high value for $R^{C_{60}}$ is obtained. Further evidence for the transition from parallel conduction dominating the resistance change to scattering dominating the change is shown in Figure 5.5. As the resistance of the underlayer is decreased $\Delta R$ becomes much smaller than $\delta R^M$, and the system resistance increases with the deposition of $C_{60}$. Because the resistance has increased, a value for $R^{C_{60}}$ cannot be calculated from Equation 2.12.

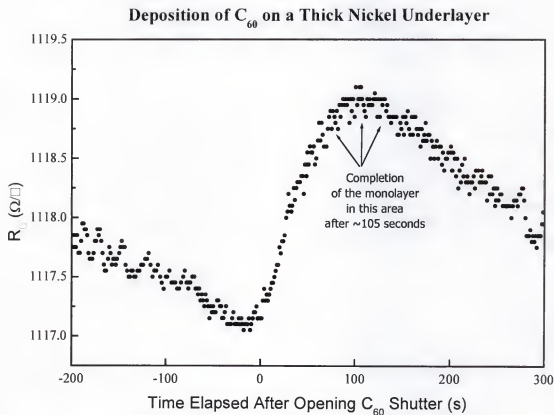Figure 5.5    Resistance increase for $C_{60}$/Ni when the nickel film is too thick. The resistance of the nickel film is small enough, and the resistance of the $C_{60}$ monolayer large enough, that the resistance increase from the scattering change is much larger than the resistance decrease from the addition of a parallel conductor. After completion of the $C_{60}$ monolayer, the resistance continues on its downward annealing trend.

### 5.1.2 Exponential Resistance Decrease

It turns out that the decrease in resistance of the $C_{60}$/Ni system with $C_{60}$-deposition-time follows an exponential curve. A simple model using only sticking probability to describe the deposition can explain this result.[78] Neglecting diffusion of the $C_{60}$ molecules about the nickel surface, we assume that if a $C_{60}$ molecule sticks to an available site on the nickel it will stay there. The probability that any given site is occupied is then given by

$$P = 1 - e^{-at} \tag{5.2}$$

where $a$ is the rate of particles sticking to the surface, and $t$ is the time elapsed. The area covered by $C_{60}$ is then

$$A' = AP = A(1 - e^{-at}) \tag{5.3}$$

where A is the surface area of the nickel film. At some sub-monolayer coverage, one can imagine the $C_{60}$ molecules gathered into a strip at one end of the nickel surface (Figure 5.6). Then the area covered by $C_{60}$ is

$$A' = ll' = l^2(1 - e^{-at}) \tag{5.4}$$

where $l$ is the width of the square of nickel surface area and $l'$ is the short dimension of the $C_{60}$-covered area. This formalism can now be used to discuss the sheet resistance of the covered and uncovered areas. With the current flowing as in Figure 5.6, aligned with the short dimension of the $C_{60}$-covered area, the number of squares of $C_{60}$/Ni is given by

$$N^{cov} = \frac{l'}{l} = 1 - e^{-at} \tag{5.5}$$

and the number of squares of uncovered nickel is given by

$$N^{\text{uncov}} = \frac{l - l'}{l} = e^{-at}. \tag{5.6}$$

The resistance of each section, covered and uncovered, is given by

$$R_{\text{cov}} = R^{\text{cov}} N^{\text{cov}} = R^{\text{cov}}(1 - e^{-at}); \quad R_{\text{uncov}} = R^{\text{uncov}} N^{\text{uncov}} = R^{\text{uncov}} e^{-at}. \tag{5.7}$$

These resistances add in series yielding the sheet resistance of the system:

$$R_{\square} = R^{\text{cov}} + (R^{\text{uncov}} - R^{\text{cov}})e^{-at}. \tag{5.8}$$

Using this model, excellent fits to the resistance change data were obtained.

Figure 5.7 shows a typical $C_{60}$ deposition fit with the function

$$R_{\square} = (1 + bt)\left[R^{\text{cov}} + (R^{\text{uncov}} - R^{\text{cov}})e^{-at}\right]. \tag{5.9}$$



a)                                    b)
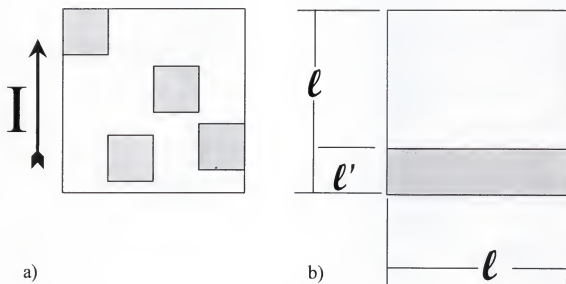
Figure 5.6    Model of the surface coverage of the metal underlayer. The large squares represent the underlayer surface. The smaller squares in 5.6a and the band across the large square in 5.6b represent the $C_{60}$.
a) Demonstration of random sticking probability on a sample. $C_{60}$ is assumed to stay in place once it sticks to the surface. b) At some sub-monolayer coverage, one can imagine the molecules gathered into a strip at one end of the nickel surface. The system is then simply two series resistors. See text for a description of the relation of coverage to resistance.

The extra $bt$ term accounts for the slight linear background of the annealing film. The excellent fit indicates there is a high sticking coefficient for $C_{60}$ on nickel, which is supported by STM[41] and spectroscopic[52, 79] experiments of sub-monolayer coverages of $C_{60}$ on nickel. It is believed there is more hybridization of the $C_{60}$ electron orbitals with the nickel surface states than is seen in $C_{60}$/(noble metal) systems (see section 5.2.2, below). This increased hybridization may also in part explain the magnitude of the $C_{60}$ sheet resistance for the $C_{60}$/Ni system. Notice also that the anneal slope before $C_{60}$ deposition is much steeper than after. The adsorption of $C_{60}$ caps the nickel surface,

**Resistance vs. Time During Deposition of $C_{60}$ on Nickel Underlayer**



Open
Shutter
to $C_{60}$

fit to $\quad R = (1 + bt)\left(R_{\square}^{cov} + \left(R_{\square}^{uncov} - R_{\square}^{cov}\right)\exp(-at)\right)$

Close shutter

$R_{\square}$ (k$\Omega/\square$)

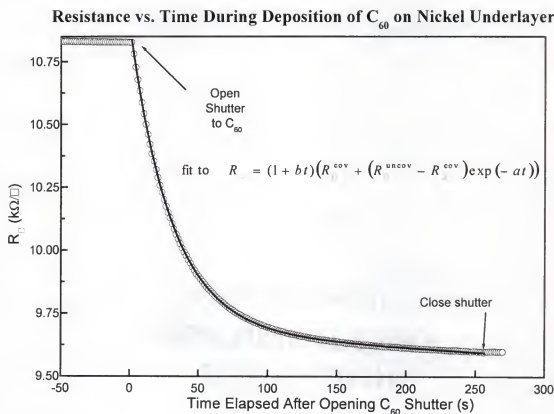Time Elapsed After Opening $C_{60}$ Shutter (s)

Figure 5.7    Coverage model fit to the exponential decay of resistance during $C_{60}$ deposition. The model described in the text and depicted in Figure 5.6, fits the data exceptionally well, indicating a strong interaction between the nickel surface and the $C_{60}$. Such a strong interaction is also supported by STM[42] and spectroscopic[53, 80] measurements.

halting the change in film resistance due to exposure to residual gasses in the chamber. The $C_{60}$ may also hinder any surface reconstruction of the nickel that may contribute to the change in resistance.

## 5.2 The $C_{60}$/Cu System

All of the $C_{60}$/Cu samples were grown in SHIVA using a magnetron sputter gun for copper deposition and a Radak resistively-heated crucible for the $C_{60}$ source. Many samples were grown, under varying conditions, before the final procedure was adopted. This procedure is as follows: The $C_{60}$ source is outgassed at 460ºC while the residual gasses in the chamber are monitored by a residual gas monitor (RGA). When the RGA spectrum has settled back down to what it was before outgassing of the $C_{60}$, the sample deposition can begin. The substrate is first lightly sputter-cleaned with an argon ion beam of 3.5 mA at 200 V for one minute. The purpose of this cleaning is to remove any adsorbents from the glass and contact pads, and to provide a smoother substrate to enhance the copper film quality. This assumption is supported by observation in an optical microscope. There is a definite demarcation between the area of the substrate exposed to the ion cleaning and the unexposed area. The unexposed surface looks rough and spotted, whereas the exposed area shows no visible roughness.

Immediately after the ion cleaning, the sample is rotated to face the copper source, the argon flow is switched to the sputter gun, and the plasma is ignited. It takes around two minutes to set up the source and begin the LabVIEW Virtual Instrument (VI) that records the resistance during deposition. Once the VI is running and the sputter gun has stabilized, the shutter is opened to deposit the copper. The deposition is stopped when a target thickness, monitored by the IC5 deposition controller, is reached. When the target

thickness is reached, as quickly as possible the sputter gun is turned off, the argon inlet valve closed, the sample rotated to face the $C_{60}$ source, and the IC5 reset to $C_{60}$ density. Then the sample shutter is opened to expose the copper substrate to the $C_{60}$ flux. The changeover process takes from one to two minutes, with an average of one hundred seconds.

### 5.2.1 Sheet Resistance of $C_{60}$

The time for changeover from the copper source to the $C_{60}$ source is crucial for obtaining a quality electron-doped $C_{60}$ monolayer. Figure 5.8 shows a plot of the $C_{60}$ sheet resistance versus the initial copper sheet resistance for all the samples in this study. The large amount of scatter in the data is due to the varying quality of the copper underlayer, controlled largely by the time between finishing the copper deposition and starting the $C_{60}$. The dashed arrow indicates the resistance of a sample whose copper underlayer was allowed to sit in the chamber for approximately twenty-four hours at a pressure of $4.5 \times 10^{-9}$ Torr, before deposition of the $C_{60}$. The growth conditions for the copper were the same as that for the sample indicated by the solid arrow, for which the time between depositions was approximately one hundred seconds. Even at such low background pressures, such a long exposure allows adsorbents to adhere to the copper that hinder the transfer of charge to the $C_{60}$, causing a difference in $C_{60}$ sheet resistance of nearly one and a half orders of magnitude. As pointed out in section 5.1.1, the underlayer metal resistance is not easily reproduced; hence, there is no statistical basis for the uncertainty in $R^{C_{60}}$. However, even if we assume an uncertainty of 95%, the two arrowed data points' uncertainties do not overlap.
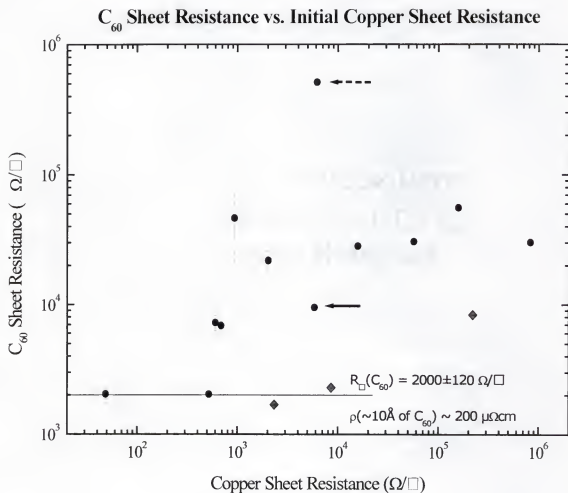
Figure 5.8    Scatter plot of $C_{60}$ sheet resistance versus copper sheet resistance. The large amount of scatter in the data is due to the varying quality of the copper underlayer. Compare the dashed-arrow data point, indicating the resistance of a sample with approximately twenty-four hours between depositions, with the solid-arrow data point, indicating a sample with only 100 seconds between depositions. The contamination of the copper surface inhibits charge transfer. The three diamond data points are for three of the four samples grown on ion cleaned substrates. For the fourth sample, the resistance increased upon deposition of the $C_{60}$; therefore, $R^{C_{60}}$ could not be calculated.

Also crucial to obtaining a high quality electron-doped monolayer of $C_{60}$ is the pre-cleaning with the sputter gun. This cleaning appears to provide a smoother copper film whose surface maximizes contact with the $C_{60}$ and thereby maximizes charge transfer. In Figure 5.8, the three diamond data points at low values of $R_{\square}^{C_{60}}$ are for three of the four samples grown on pre-cleaned substrates. For the fourth sample, the copper underlayer was too thick, resulting in an increase in resistance upon adsorption of the $C_{60}$. $R_{\square}^{C_{60}}$ could not be calculated for that sample. After a few preliminary trials of growing $C_{60}$/Cu using the pre-cleaning method which determined the optimal thickness for the copper underlayer, a sample was grown which produced an $R_{\square}^{C_{60}}$ of ~1900Ω/$\square$. The transport properties of this sample are described below.

### 5.2.2 Non-exponential Resistance Decrease

In Section 5.1.2 it was shown that a coverage model that assumed a high sticking coefficient for $C_{60}$ to nickel was very successful in fitting the resistance decrease during $C_{60}$ deposition. Figure 5.9 shows a typical resistance decrease during the deposition of $C_{60}$ on copper. Notice that the same fitting model from Section 5.1.2 does not fit the data. The deviation of the fit from the data can be explained by a higher mobility of the $C_{60}$ molecules on the surface of the copper than on the surface of nickel. STM studies have shown that $C_{60}$ is indeed quite mobile on noble metal surfaces, specifically copper, collecting at step-edges and surface defects at sub-monolayer coverages.[53, 76, 80, 81] The initial faster-than-exponential section of the data indicated by the dashed arrow in Figure 5.9 is likely due to this high surface mobility, allowing the $C_{60}$ to form a connected network more quickly than on the nickel underlayer.

**Resistance vs. Time During C$_{60}$ Growth on a Copper Underlayer**



fit to $R = (1 + bt)\left(R^{\text{cov}} + \left(R^{\text{uncov}} - R^{\text{cov}}\right)\exp\left(-at\right)\right)$

Open Shutter to C60

Close shutter

R$_{\square}$ ($\Omega/\square$)

Time Elapsed After Opening C$_{60}$ Shutter (s)
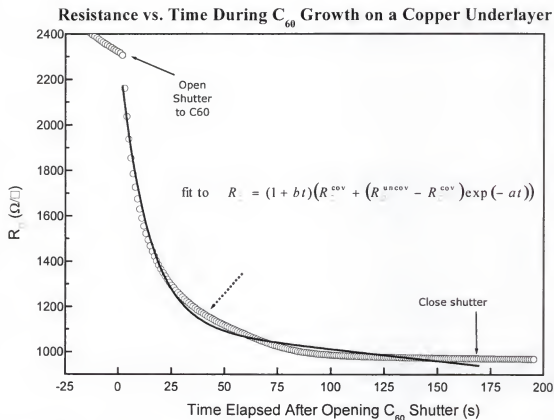
Figure 5.9     Resistance decrease for C$_{60}$/Cu. Notice the fitting model that was so successful for C$_{60}$/Ni falls short here. The increased mobility of C$_{60}$ on the surface of noble metals may explain the somewhat faster-than-exponential region of the data indicated by the dashed arrow.

### 5.2.3   Resistance as a Function of Temperature

Upon completion of the final C$_{60}$/Cu film with $R^{C_{60}} \sim 1900\Omega/\square$, the sample was moved immediately into the ShivaStat and resistance versus temperature measurements were begun, as described in section 4.2.1. Figure 5.10 shows the normalized sheet resistance versus log(T) for sample C$_{60}$/Cu 012501 before and after exposure to air for approximately 30 seconds. This data is a compilation of several sweeps of temperature taken over twelve days. There was some trouble with the magnet in the ShivaStat, which

prolonged the measurements of the sample. For each attempt at collecting

magnetoresistance data, temperature data was gathered. Above 55 K, the sample shows

metallic temperature dependence, decreasing linearly as temperature decreases. Below

the minimum at 55 K, the resistance increases as -ln(T), consistent with weak localization

as applied to disordered copper films.[82] The increase in resistance of the sample after

venting is consistent with destruction of the conducting $C_{60}$ monolayer and the addition of
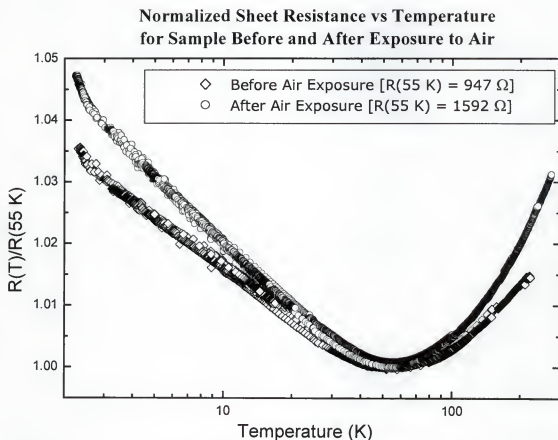


Figure 5.10    $C_{60}$/Cu normalized sheet resistance versus temperature before and after venting. The destruction of the conducting $C_{60}$ layer by exposure to oxygen does not change the qualitative behavior of the system. The above-55 K region is still metallic, though the slope is roughly twice that of the pre-vent data. Again, below 55 K, the post-vent data shows a slope roughly twice that of the pre-vent. The resistance of the sample changed by about 50% after venting.

an oxidized copper layer on top of the copper underlayer. This oxidized layer would likely be very rough, increasing the diffusivity of scattering from the interface. The increase in scattering at the interface of $C_{60}/Cu$ could explain the change of about a factor of two in the slope of $R$ versus log(T).

As discussed in Section 3.1, the slope of the $G$ versus log(T) curve is an indication of the scattering mechanism for the system. Figure 5.11 shows the normalized sheet conductance versus log(T) for the same sample before and after air exposure. For the normalization calculation (Equation 3.5), $G$ (55 K) was used as the classical resistance in $\Delta G$. The scaling at $T > 55\ K$ of the pristine and vented data indicates that only the weak localization temperature regime is affected by the loss of the conducting $C_{60}$. Fitting the normalized data with Equation 3.5 yields values for $p$ of 0.967±0.001 and 0.713±0.001 for the pre-vent and post-vent data, respectively. Note there is an inflection in the data at approximately 2.5 K. This inflection may indicate a change in the dephasing mechanism for the system. The above-mentioned $p$ values were obtained by fitting to temperatures above this inflection (~3–30 K). The data below the inflection point were not fit, due to a paucity of data points in that region. Recall from Section 3.1 that $p = \alpha P$, where $\alpha$ is determined by film morphology and $P$ is determined by the dephasing mechanism for the conduction electrons. In the next section, the value for $\alpha$ is determined from magnetoresistance. The discussion of the $p$ data continues there.

**Normalized Sheet Conductance versus Temperature, With Fits**

Legend:
- ○ Pre-Vent Data
- ——— Fit of Pre-Vent  p=0.997±0.002
- ◇ Post-Vent Data
- – – – Fit of Post-Vent  p=0.713±0.002

Y-axis: $\Delta G / G_{00}$

X-axis: Temperature (K)

fit to $\dfrac{\Delta G}{G_{00}} = p\ln(T) + const.$
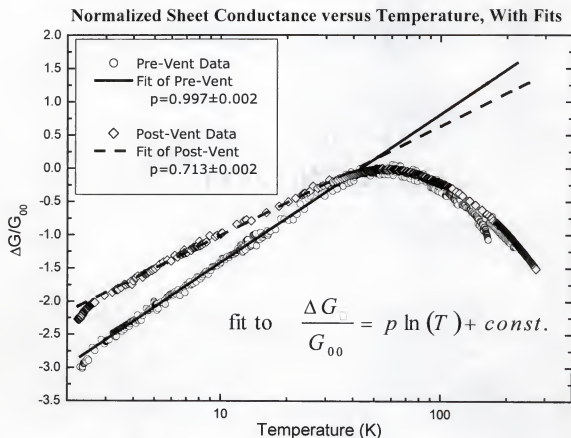
Figure 5.11    $C_{60}$/Cu normalized sheet conductance versus temperature before and after venting. Above 55 K the sample shows metallic behavior, with conductance increasing roughly linearly as temperature decreases. Below the minimum, the conductance decreases as ln(T), consistent with weak localization theory. Fits to Equation 3.5 were used to obtain the values of $p$ in the legend. Electron-electron dephasing interactions are usually associated with a $p$ value of one.[68] $\Delta G$ is calculated using G(55 K) for $G_0$.

**5.2.4  Magnetoresistance**

Figure 5.12 shows the 2.3 K magnetoresistance for $C_{60}$/Cu.  During ramping of

the magnet, the temperature of the sample drifted, due to eddy current heating in the

copper parts of the cryostat system.  The effect of this drift is seen in the open-circle data.

The sample is clamped to a copper disk, which is part of the transfer pod assembly.  The

pod-receiver is a large copper annulus, with few holes in it to disrupt any eddy currents.

The sample itself may also develop eddy currents.  All of these extra currents provide

added heat loads to the cooling system.  For high magnet ramp rates, especially at the

**2.3 K Magnetoresistance for $C_{60}$/Cu**
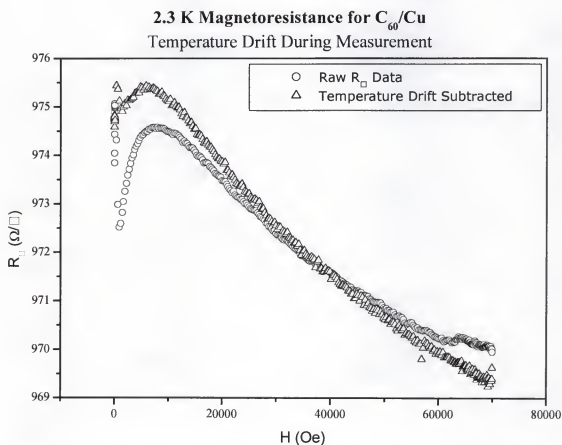
Temperature Drift During Measurement



Figure 5.12    Raw and temperature-corrected magnetoresistance of $C_{60}$/Cu.  Eddy-current heating in the sample and copper parts of the transfer pod and pod-receiver causes a temperature drift during ramping of the magnet.  The temperature dependence is subtracted from the open-triangle data.

bottom end of the temperature range, this extra load is enough to change the temperature of the sample significantly. For the measurements shown here the ramp rate was approximately 50 Oe/s, at low fields. At higher fields, the ramp rate reduced as the magnet controller reached its peak output voltage. Efforts are underway to reduce the eddy-current heating by redesigning the pod-receiver to include more eddy-damping slots.

To remove the effects of temperature drift from the magnetoresistance, the low-temperature R-versus-T data were fit to a ln(T) dependence, which was then subtracted
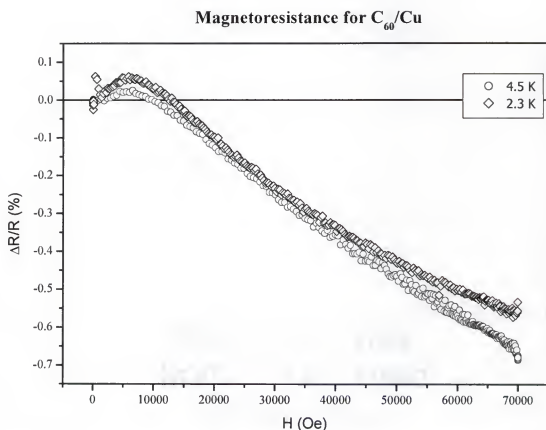
### Magnetoresistance for $C_{60}$/Cu



Figure 5.13    $C_{60}$/Cu magnetoresistance at 2.3 K and 4.5 K. The initial positive magnetoresistance is consistent with spin-orbit coupling. The subsequent turn over to negative magnetoresistance can be explained by weak localization. The data follows the form of the digamma function (Equation 3.6) after turnover.

from the raw magnetoresistance data (open-triangle data). Figure 5.13 shows a plot of

sheet resistance versus magnetic field at 2.3 K and 4.5 K for the $C_{60}$/Cu with the

temperature drift removed from both. The initial positive magnetoresistance is consistent

with spin-orbit coupling. The crossover to negative magnetoresistance is consistent with

weak localization, as discussed in Section 3.1.



**Normalized MagnetoConductance for $C_{60}$/Cu**

- ○ 4.5 K
- — Fit to 4.5 K Data
  $H_\phi$ = 9000 Oe, $\alpha$ = 0.9
- ◇ 2.3 K
- – – Fit to 2.3 K Data
  $H_\phi$ = 8900 Oe, $\alpha$ = 0.8

fit to $\dfrac{\Delta G}{G_{00}} = \alpha \left[ \Psi\left( \dfrac{1}{2} + \dfrac{H_\phi}{H} \right) - \ln\left( \dfrac{H_\phi}{H} \right) \right]$

(y-axis) $\Delta G / G_{00}$

(x-axis) H (Oe)

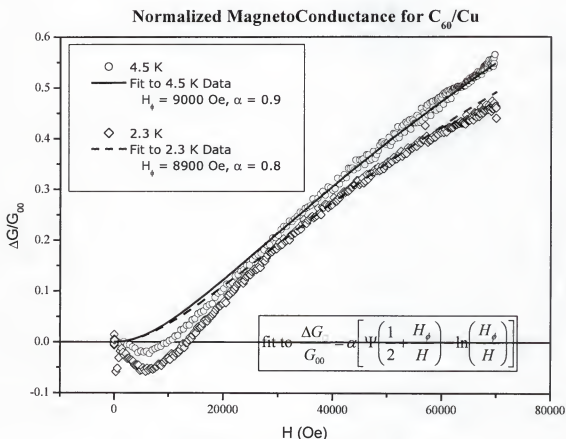Figure 5.14    Normalized magnetoconductance with fits. The 4.5 K data fit fairly
well to Equation 3.6, though the 2.3 K data do not. There was a lot of
temperature drift in the data from inductive heating during magnet
ramping. This drift has been subtracted, but the deviations from the fit
may be related to this problem. Unfortunately, the correction of the
data adds extra uncertainty to any fitted values.

Figure 5.14 shows the normalized magnetoconductance (Equation 3.6), for $C_{60}$/Cu. Fitting with Equation 3.6 yields values for $H_\phi$ of 8900 Oe and 9000[3] Oe, and values for $\alpha$ of 0.8 and 0.9, for 2.3 K and 4.5 K, respectively. These values of $H_\phi$ correspond to values for $L_\phi$ of approximately 136 Å and 135 Å at 2.3 K and 4.5 K, respectively. Given the noise in the data, and the problems with temperature drift, these values are probably only good to 10%. The total conducting film is only around 55 Å thick (45 Å of copper and 10 Å of $C_{60}$). Therefore, as far as phase breaking events are concerned, the system is approximately two-dimensional. Recall that $\alpha$ is dependent upon the strengths of spin-orbit and magnetic scattering. A value for $\alpha$ of one is consistent with an absence of both spin orbit interactions and magnetic scattering.[70]

Recall from Section 5.2.3 that only one region of the conductance versus temperature data was fit (~3–30 K). Combining the value for $p$ from that fit (0.967) with the 4.5 K value for $\alpha$ yields a value for $P$ of 1.07. $P = 1$ is associated with phase-breaking dominated by electron-electron interactions in disordered , or 'dirty', 2D films.[83-85] The decrease from one of the post-vent $p$-value may indicate a change in $\alpha$ for the sample. Unfortunately, a problem with the ShivaStat magnet prevented the taking of data after exposing the sample to air. Nevertheless, if $P$=1 is assumed, the post-vent value for $p$ indicates that $\alpha$ decreases by a factor of about 0.8 upon destruction of the conducting $C_{60}$ monolayer.

CHAPTER 6
THE $C_{60}$:$Ni_x$ COMPOSITE FILMS

The work on $C_{60}$:$Ni_x$ composite films is an extension of the $C_{60}$/Ni studies. The motivation is to study the transport properties of electron-doped $C_{60}$ in a disordered composite. While the electron-doped $C_{60}$ monolayers are 2D systems, the doped $C_{60}$ in these composites is quasi-2D. The charge transfer is still limited to the 2D layer in contact with nickel, but the conducting $C_{60}$ monolayers are part of a larger, extended matrix, like a 3D array of conducting bubbles in a non-conducting medium. These bubbles are filled with yet another conducting medium—nickel. This chapter covers the characterization of these composite samples, and is divided into four sections: growth and morphology, resistance versus temperature, Hall effect, and magnetoresistance measurements.

## 6.1 Growth and Morphology

Through the course of the work, four samples were grown and characterized. The first three samples were grown in the Oz system, while the fourth was grown in SHIVA. The reason for the switch is that in SHIVA it is possible to move the thickness monitor so that the Omicron EF3 is depositing directly upon it. In this way, the mass ratio of $C_{60}$ to nickel can be determined without the need to recalibrate flux measurements each time a new filament is used in the EF3. Table 6.1 lists the totality of samples with their corresponding number ratios of $C_{60}$:$Ni_x$, their resistivities upon completion of the growth,

Table 6.1        Table of composite samples listing $C_{60}:Ni_x$ ratios, end-growth resistivity, thickness, and growth chamber.

| Sample Name | x | $\rho$ ($\mu\Omega\cdot$cm) | d (Å) | Chamber |
|---|---|---|---|---|
| $C_{60}:Ni_{23}$ (041000) | 23±3 | 1200±100 | 300±30 | Oz |
| $C_{60}:Ni_{21}$ (081000) | 21±2 | 270±30 | 72±7 | Oz |
| Nickel (052600) | NA | 150±20 | 38±4 | Oz |
| $C_{60}:Ni_{90}$ (101800) | 90±1 | 100±10 | 130±13 | SHIVA |

their thicknesses, and in which chamber they were grown. The first three composites were grown such that their resistances upon completion of the growth were nearly equal. The second and third films ($C_{60}:Ni_{21}$ and the pure nickel film) seem to be of much better quality than the first, so their resistivities and thicknesses are comparable. The first film was grown under more unstable conditions; consequently, it is more disordered and heterogeneous, with a much higher resistivity and larger thickness

A typical composite growth is shown in Figure 6.1. Note that the composite film begins to conduct, likely in the hopping regime, at around 70 s, well before a pure nickel film grown at a similar rate does (~200 s, see Figure 5.1). This early connection compared to pure nickel is true of all the composite films. The $C_{60}$ may be providing extra nucleation sites, as well as filling in gaps in the nickel with conducting $C_{60}$.

The structure of the films is such that the nickel forms islands inside the host $C_{60}$ matrix. This interpretation is based on the idea that the cohesive energy of the transition metals is too high to allow dispersion of the metal into the interstitial sites of the $C_{60}$. Instead, the nickel forms small islands that grow and push aside the $C_{60}$ during deposition. There is direct evidence for this with $C_{60}:Co$ and $C_{60}:Fe$ composite films,[86]

where the authors see columnar grains of cobalt and iron interspersed with $C_{60}$. Because of the similarity of iron, cobalt, and nickel, it is safe to assume that $C_{60}:Ni_x$ also comprises these columnar grains surrounded by a web of $C_{60}$; however, TEM (Transmission Electron Microscopy) measurements should be performed to verify this assumption. Figures 6.2–6.6 show AFM (Atomic Force Microscopy) topography scans of the surface of the four films listed in Table 6.1. The nickel film (Figure 6.2) seems to
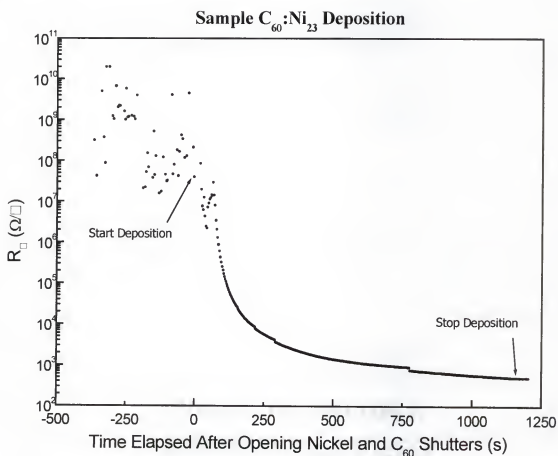


Figure 6.1      Deposition of $C_{60}:Ni_{23}$ sample. The behavior shown here is typical of the three composites. The addition of the $C_{60}$ efflux seems to cause the film to connect electrically much sooner ($\sim 70$ seconds) than for nickel alone ($\sim 200$ seconds). The $C_{60}$ may be providing extra nucleation sites for the nickel, or bridging the gaps between nickel islands, lowering the hopping barrier.

consist of a thin layer of nickel, on the order of 40 Å, with large grains, ranging from tens of Ångstroms to hundreds of Ångstroms high, in a percolating pattern. The rms roughness of the surface is ~150 Å, though the roughness in the smooth, thin-nickel regions is only ~30 Å. It appears the nickel is very mobile on the glass, collecting into large grains while forming an underlying thin layer. The inhomogeneity of the sample is likely caused by a dirty substrate. The grain structures look suspiciously like water spots. It may be that the substrate was poorly prepared, or that it was somehow contaminated *in situ*.

The $C_{60}:Ni_{23}$ film was grown under the same conditions as the nickel film, but its surface is much different. There are two regions of the film surface where the morphology differs greatly. At one end of the sample, near one current electrode, there
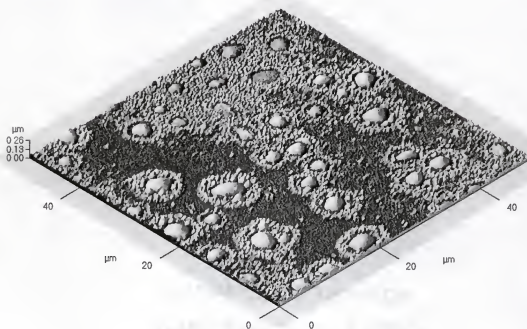


Figure 6.2    Surface topography of nickel. Scan size is 50 μm; RMS roughness is 154 Å. The inhomogeneity of the system may be the cause of the high resistivity.

are large pancake structures (Figure 6.3), which seem to be grains of either the nickel or the $C_{60}$. The surface in this region is relatively smooth (~50 Å) compared to the other end of the sample, which is very rough (~170 Å) with many small grains (Figure 6.4). It is impossible to tell with the AFM if these grains are nickel or $C_{60}$. The gradient of grain sizes is not understood, though it could be that the glass surface had a gradient of nucleation sites across it. The large pancakes could be in a region of low nucleation site density. If the nickel is mobile enough within the composite, then it could collect into large islands. If, at the other end of the sample, there were more nucleation sites, the nickel would not have migrated far enough to form large islands. In addition, the nickel flux during the $C_{60}:Ni_{23}$ deposition was very unstable. At some points during the growth, the flux dropped drastically, so there may be layers of the film with more $C_{60}$ than indicated by the nominal stoichiometry.

The third and final sample grown in the Oz system, $C_{60}:Ni_{21}$, is shown in Figure 6.5. The sample is over all relatively smooth, but there are large grains of what is probably nickel, scattered about the surface, which raises the rms roughness to ~100 Å. The nickel source may have been spitting a little during deposition, as the large grains are rare. For emphasis, the scan with the highest number of large grains is shown.

The fourth sample, grown in SHIVA, is of much better quality than the other three. Its rms roughness is only 15 Å, and the nickel and $C_{60}$ seem well dispersed across the surface (Figure 6.6). This is easily the most homogeneous sample, which may play a role in explaining its magnetoresistance compared to the other samples (see Section 6.3). It also has the lowest resistivity of the four. The only difference in growth conditions is that it was grown in SHIVA in a much cleaner vacuum.
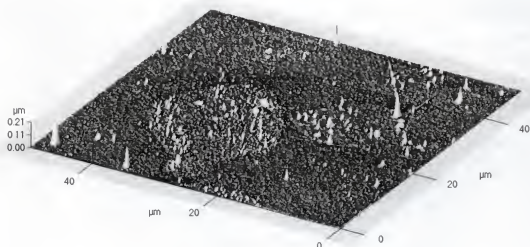
Figure 6.3    Surface topography of $C_{60}:Ni_{23}$. Scan size is 50 μm; RMS roughness is 52 Å. There are two regions of the sample with differing roughnesses. This is a picture of the smoother end. It is unknown how the film developed such a roughness gradient.



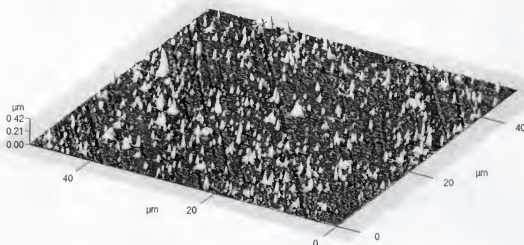Figure 64    Surface topography of $C_{60}:Ni_{23}$. Scan size is 50 μm; RMS roughness is 174 Å. Scan two on $C_{60}:Ni_{23}$ shows the rougher end of the sample. AFM topography is unable to determine whether the bumps are $C_{60}$ or nickel grains.
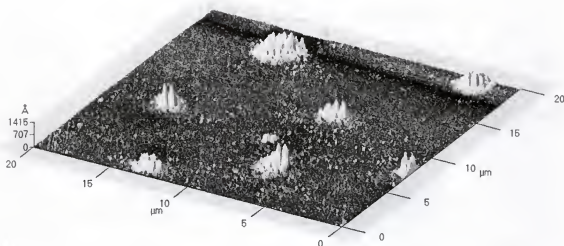
Figure 6.5    Surface topography of $C_{60}$:$Ni_{21}$. Scan size is 20 μm; RMS roughness is
104 Å.  The large grains are most likely congregated nickel.  Perhaps
the source was spitting during deposition, allowing large amounts of
nickel to strike the surface in some areas.  This scan is of an area of
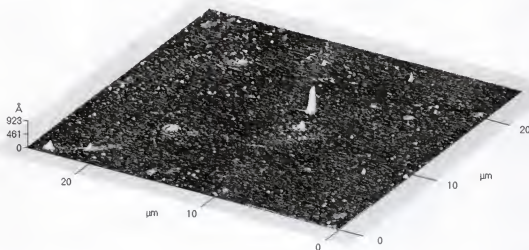high lump density.



Figure 6.6    Surface topography of $C_{60}$:$Ni_{90}$. Scan size is 25 μm; RMS roughness is
15 Å.  The cleanest and smoothest of the samples, $C_{60}$:$Ni_{90}$ has a
roughness comparable to a smooth $C_{60}$ film (~20 Å).

## 6.2   Resistance as a Function of Temperature

Figure 6.7 shows the sheet resistance as a function of temperature for the three composites normalized to their 300 K resistances.  Upon inclusion of $C_{60}$ with the nickel, the samples exhibit a negative temperature coefficient at low temperatures, with as little as 1% $C_{60}$ by number (40% carbon).  Depending on the ratio of nickel to $C_{60}$, the resistance may decrease somewhat, like a metal, before reaching a minimum ($C_{60}:Ni_{90}$),

**Normalized Sheet Resistance vs. Temperature for $C_{60}Ni_x$**



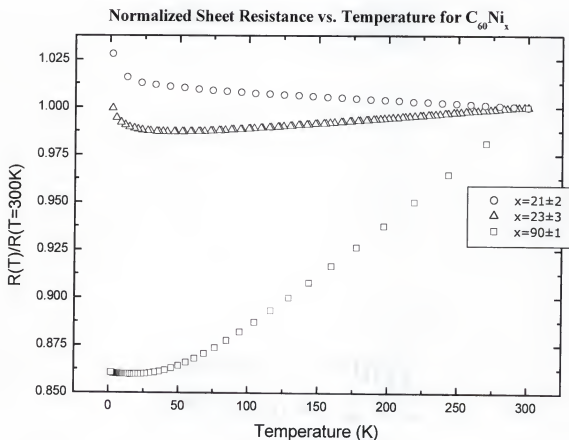| | |
|---|---|
| ○ | x=21±2 |
| △ | x=23±3 |
| □ | x=90±1 |

Figure 6.7    Normalized sheet resistance as a function of temperature for the three composite $C_{60}:Ni_x$ films.  Resistance is normalized to the 300 K resistance value.  All three composites exhibit upturns to insulating behavior at low temperature.  No saturation of resistance is seen at the available temperatures.

or increase for all temperatures ($C_{60}$:$Ni_{23}$). At the available temperatures, the resistance does not saturate.

### 6.3 Hall Effect

Hall effect measurements were performed on all samples from 5–300 K in fields of -7–7 T. The data from these measurements are grouped in Figures 6.8–6.14. All samples showed evidence of ferromagnetism in that they exhibited the anomalous Hall effect at all measured temperatures. For each sample, the magnitude of the anomalous Hall effect increased as temperature decreased (see Figures 6.8–6.11). However, $C_{60}$:$Ni_{90}$ showed a tighter grouping of curves spanning the 5–300 K temperature range (Figure 6.9). This is in contrast even to the pure nickel film, which behaves more like $C_{60}$:$Ni_{21}$ and $C_{60}$:$Ni_{23}$. Perhaps since the $C_{60}$:$Ni_{90}$ film is more homogeneous than the others, it is easier for it to spontaneously magnetize. This could explain why the higher temperature curves lie so close to the 5 K curve. Figure 6.12 shows the 5 K $R_S M$ "magnetization" of the four samples, determined by subtracting the $R_0 H$ component from the Hall resistivity. The $R_S M$ curves appear to track with the resistivity of the composites, though the nickel film does not fit the trend. It may be that $R_S$ depends largely on the disorder of the system.

From the fits to the high-field region of the Hall resistance, values for the Hall carrier density and mobility at various temperatures were obtained. These data are presented in Figures 6.13 and 6.14. The carrier densities are roughly metallic, on the order of $10^{23}$ cm$^{-3}$. The carrier densities of the composites follow the same trend as the resistivity of the samples. In other words, the most resistive sample has the lowest carrier density, and vice versa, but the mobilites do not follow that trend.

**Hall Resistivity For Nickel**

| | |
|---|---|
| ○ | 5 K |
| ☆ | 79 K |
| ◇ | 153 K |
| ◇ | 226 K |
| △ | 300 K |
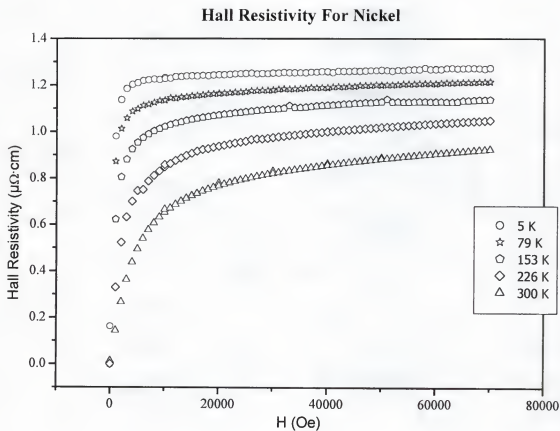
Figure 6.8   Hall resistivity for pure nickel sample.  The sample demonstrates the typical ferromagnetic anomalous Hall effect (Section 3.2)
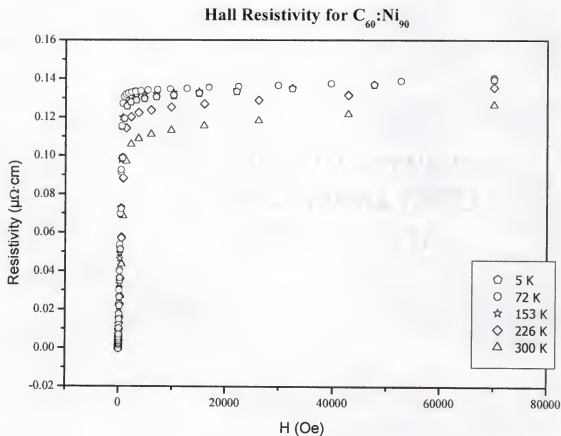
Figure 6.9   Hall resistivity for $C_{60}:Ni_{90}$. Note the curves lie closer together than for any of the other three samples. The more homogeneous distribution of nickel grains throughout the sample probably allows for spontaneous magnetization to occur more easily.

**Hall Resistivity for C$_{60}$:Ni$_{21}$**
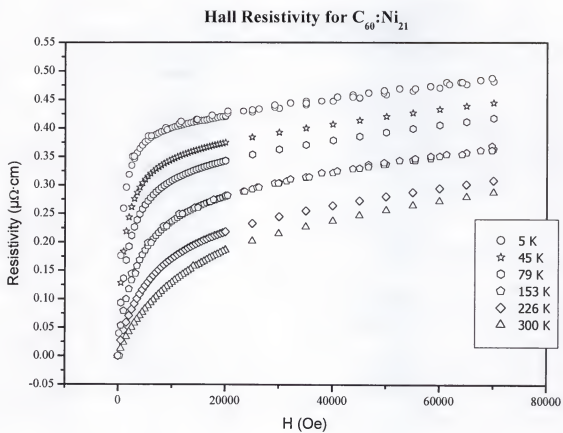


Figure 6.10    Hall resistivity for C$_{60}$:Ni$_{21}$.
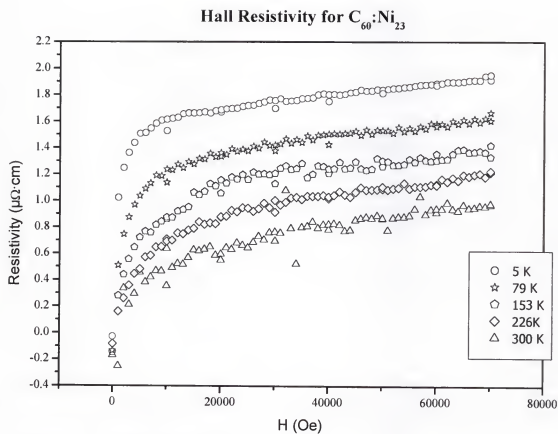
Figure 6.11    Hall resistivity for $C_{60}:Ni_{23}$.

**5 K "Magnetization" for Nickel and C$_{60}$:Ni$_x$**

*y-axis:* $R_S$·M ($\mu\Omega$·cm)

*x-axis:* H (Oe)

Legend:
- △ C$_{60}$Ni$_{23}$, $\rho$ = 1200 $\mu\Omega$·cm
- ◇ Nickel, $\rho$ = 150 $\mu\Omega$·cm
- ○ C$_{60}$Ni$_{21}$, $\rho$ = 270 $\mu\Omega$·cm
- ○ C$_{60}$Ni$_{90}$, $\rho$ = 100 $\mu\Omega$·cm
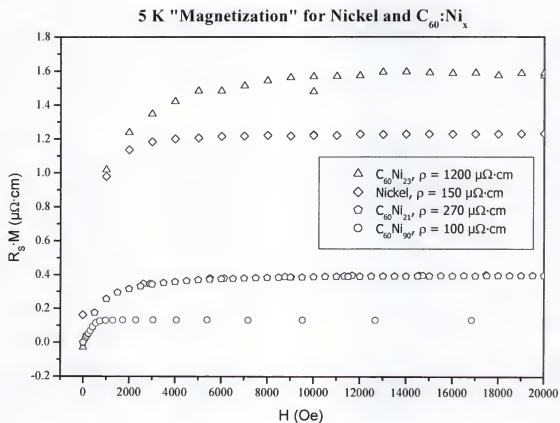
Figure 6.12    5 K "magnetization" for nickel and C$_{60}$:Ni$_x$. The $R_S M$ curves for the composites follow the trend of the resistivities. Only the data up to 2 T is shown, to highlight the low field curvature.

Figure 6.13    Hall carrier density for nickel and $C_{60}$:$Ni_x$. The carrier density is lowest for the highest resistivity composite, and tracks with the resistivity trend.
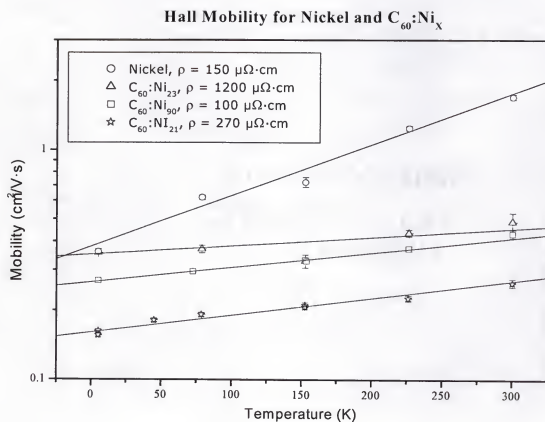
Figure 6.14    Hall mobility for nickel and $C_{60}$:$Ni_x$.  Unlike the carrier density, the composite mobilities do not track with the resistivities of the composites.

## 6.4 Magnetoresistance

The magnetoresistance measurements of a pure nickel film and of the $C_{60}:Ni_x$

composites are grouped in Figures 6.15–6.27. Measurements were made at temperatures

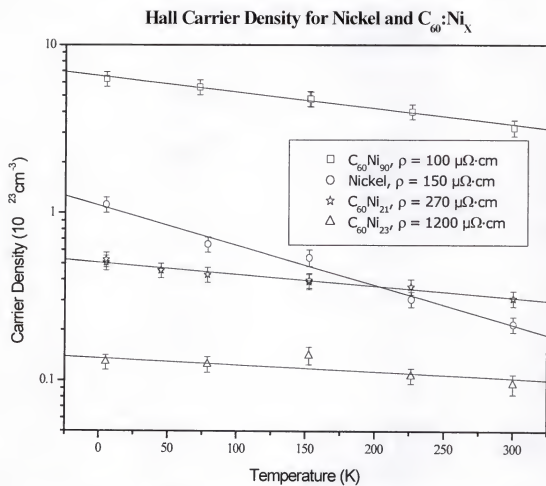ranging from 5–300 K. The transverse magnetoresistance of the nickel film shows a

suppression after magnetization saturation as temperature decreases. This suppression

**Transverse Magnetoresistance for Nickel**



Figure 6.15    Transverse magnetoresistance of a nickel film. The film is around 40 Å
thick, but is very disordered (see Figure 6.2). The noise is due
primarily to problems with the PPMS AC resistance bridge and
common mode rejection. Despite the noise at 5 K, there appears to be
the expected turn to positive magnetoresistance discussed in Section
3.1, as evidenced by the suppression of magnetoresistance after

may be the advent of the crossover to positive inflection for ferromagnets discussed in
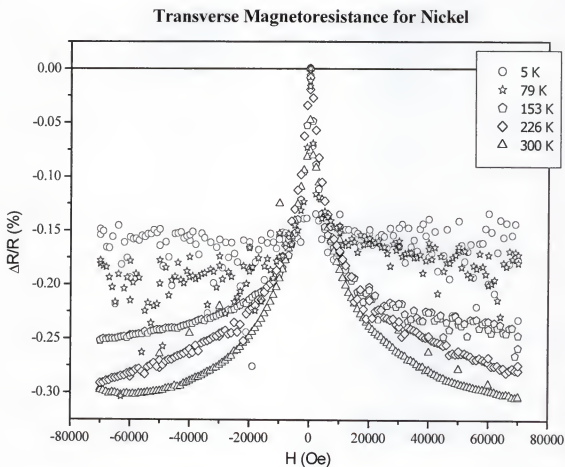
Section 3.1. The magnetic field was first swept from 0 T to 7 T, then to -7 T, and finally

back to 0 T. For the three composites the transverse magnetoresistance undergoes a

change from the negative magnetoresistance typical of a ferromagnetic material (Figure

6.15), to a positive magnetoresistance. It is not uncommon for pure ferromagnetic

materials to cross over to classical $H^2$ dependence at low temperatures;[64] however, the

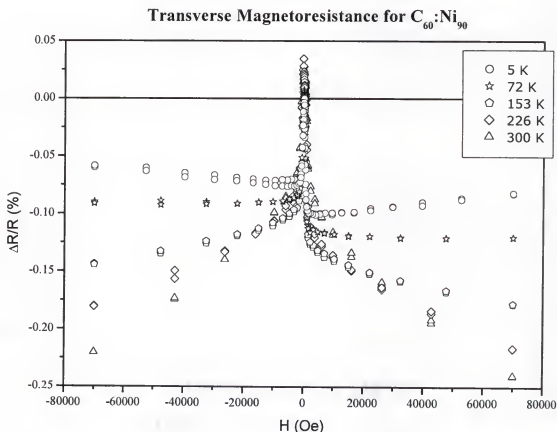magnitudes of the magnetoresistance in the two temperature regimes are usually similar.



Figure 6.16    Transverse magnetoresistance of $C_{60}$:$Ni_{90}$. Notice the sharpness of the
central peak indicating rapid saturation of magnetization (Shown in
close up in Figure 6.12). Notice also the crossover to slightly positive
magnetoresistance at low temperature typical of ferromagnetic
materials.[64]

The $C_{60}$:$Ni_{90}$ sample, for example, shows only a slight turn up after saturation of the magnetization (Figure 6.16). The pure nickel sample (Figure 6.15) shows suppression of magnetoresistance but no turn up to positive slope. It is, therefore, intriguing that the magnitude of the positive magnetoresistance at low temperatures is so large in samples $C_{60}$:$Ni_{21}$ and $C_{60}$:$Ni_{23}$. The crossover temperature seems to vary roughly inversely with the nickel concentration, being around 200 K for x = 21, 23, and around 70 K for x = 90. Note, though, that the $C_{60}$:$Ni_{90}$ crossover is likely due to typical ferromagnetic behavior. Hence, with only two samples, a trend can not be determined.

For samples $C_{60}$:$Ni_{90}$ and $C_{60}$:$Ni_{21}$, the difference at low fields between the longitudinal magnetoresistance (Figures 6.17 and 6.23) and the transverse magnetoresistance (Figures 6.16 and 6.22) can be attributed to anisotropic magnetoresistance (AMR), which is common in ferromagnetic materials. Anisotropic magnetoresistance is a result of a difference in spin-orbit coupling when the current is perpendicular and parallel to the magnetization.[64, 65] As discussed in Section 3.1, after the sample magnetization has saturated, there should be little or no difference between the longitudinal and transverse orientations, unless orbital effects, which would be prominent in the transverse direction only, contribute to the magnetoresistance.[87, 88] This holds true for $C_{60}$:$Ni_{90}$ and $C_{60}$:$Ni_{21}$ samples. For fields greater than 1 T the curvature of the data is the same for either configuration. The similarity of the data from the two orientations indicates that there is little contribution to the magnetoresistance from orbital effects.

At low fields (0–2500 Oe), the $C_{60}$:$Ni_{90}$ sample showed hysteresis effects in the magnetoresistance (Figures 6.18, 6.20, 6.21), which may be associated with ferromagnetism. The nickel film does not show such hysteresis; however, similar effects

**Longitudinal Magnetoresistance for $C_{60}$:$Ni_{90}$**

ΔR/R (%)

H (Oe)

| | |
|---|---|
| ○ | 5 K |
| ☆ | 72 K |
| ○ | 153 K |
| ◇ | 226 K |
| △ | 300 K |
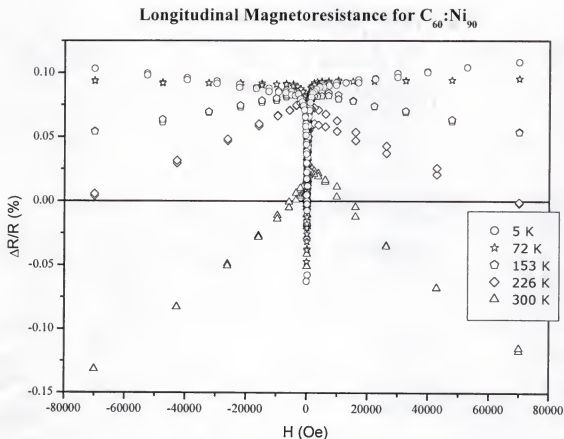
Figure 6.17    Longitudinal magnetoresistance for $C_{60}$:$Ni_{90}$. This sample exhibits the anisotropic magnetoresistance typical of ferromagnets. Notice that after saturation the magnetoresistance curve follows that of the transverse orientation

have been seen in discontinuous, granular nickel films[89] in the superparamagnetic regime. These films exhibit single-peaked negative magnetoresistance until they reach a certain thickness, where the domains can couple. Perhaps the inhomogeneity of the nickel film grown for this work pushes it into the superparamagnetic regime.

It is possible that the peaks shown in Figure 6.18 coincide with the points of zero magnetization of the sample. Attempts to measure the magnetization of the sample directly in a SQUID magnetometer were unsuccessful. The films were too thin to provide

# Transverse Magnetoresistance Hysteresis for $C_{60}:Ni_{90}$
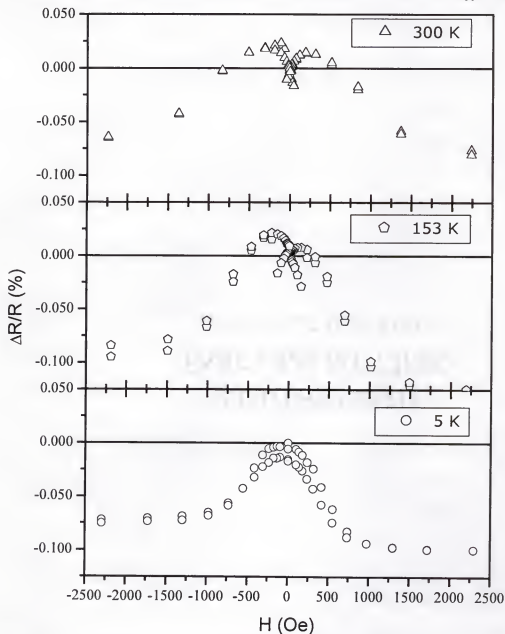


Figure 6.18    Transverse magnetoresistance for $C_{60}:Ni_{90}$, from -0.25–0.25 T. The central peak is much sharper than for the nickel film. This is likely due to the $C_{60}:Ni_{90}$ being a more homogeneous film. Two positive magnetoresistance hysteresis bumps can be seen around |250| Oe. These bumps probably correspond to the points of zero magnetization in the hysteresis curve, as expected for a ferromagnet. However, one would expect the coercive field to increase as temperature decreases. Here it appears to decrease, and even disappear at 5 K. A secondary hysteresis appears below 250 Oe, which is shown in Figure 6.20.

enough signal to overcome the diamagnetic signal of the substrate. If the peaks in the transverse magnetoresistance coincide with zero magnetization, one would expect the coercive field to increase with decreasing temperature. However, the peaks in Figure 6.18 move to lower fields as temperature decreases. Since the Hall effect indicates ferromagnetism at all temperatures, the magnetic softening of the material is not understood.

In Figure 6.20, a secondary hysteresis in the transverse magnetoresistance of $C_{60}:Ni_{90}$ is shown. As the field is swept up from 0 T, the magnetoresistance is initially slightly negative. Then the curve abruptly jumps to a positive magnetoresistance and follows the peak shown in Figure 6.18. Upon returning from 7 T through 0 T, the magnetoresistance is again slightly negative and again jumps abruptly to the positive peak shown in Figure 6.18. Upon returning from -7 T, the curve goes smoothly to zero. This hysteresis does broaden as temperature decreases, but it begins to disappear for the 72 K data, and is nowhere in evidence at 5 K. Similarly for the longitudinal magnetoresistance (Figure 6.21), a hysteresis exists at low fields. The behavior as temperature decreases is different than for the transverse orientation. For the longitudinal orientation, the hysteresis disappears at intermediate temperatures, then reappears for the low temperature data. It is unknown why the hysteresis minima would disappear at all, much less at different temperatures for the different orientations.

It is interesting to note there is a suppression of the longitudinal, and an enhancement of the transverse, anisotropic magnetoresistance at 5 K in $C_{60}:Ni_{21}$. The cause of the deviation from ferromagnetic anisotropic magnetoresistance at low temperature in this sample is unknown. Unfortunately, no data were taken in the

longitudinal orientation for $C_{60}:Ni_{23}$, but the transverse low-field magnetoresistance does seem to be slightly enhanced at low temperatures. A more in depth study of the low temperature low field properties of these composites may reveal some interesting physics.

Recently data has been published which may help explain the high field behavior of the magnetoresistance for $C_{60}:Ni_{21}$ and $C_{60}:Ni_{23}$ at low temperatures. Manyala *et al.* report a similar crossover to positive magnetoresistance in $Fe_{1-x}Co_xSi$,[88] which they attribute to the Coulomb interaction enhanced by quantum mechanical interference, akin to that seen at 1 K in Si:P by Rosenbaum *et al.*[90] Manyala *et al.* suggest that the high crossover temperature compared to that of Si:P is due to the large internal magnetic fields provided by the ferromagnetic dopants. There are a few similarities between $C_{60}:Ni_x$ and $Fe_{1-x}Co_xSi$ which suggest the physics of the crossover might be similar. Both $C_{60}:Ni_x$ and $Fe_{1-x}Co_xSi$ have insulating, electron correlated hosts—$C_{60}$ and FeSi. Both systems have magnetic dopants, and both exhibit a crossover to large positive magnetoresistance with a roughly linear dependence on $\vec{H}$. However, the inhomogeneity of the $C_{60}:Ni_x$ samples could play an important role in the magnetoresistance, as grain-boundary scattering can also provide positive magnetoresistance.[88] Further study of the $C_{60}:Ni_x$ system using TEM to determine the homogeneity of the samples may help settle the question.
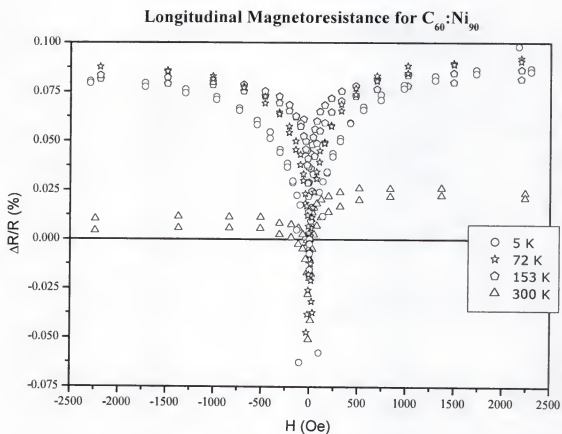
Figure 6.19   Longitudinal magnetoresistance for $C_{60}:Ni_{90}$, from -0.25–0.25 T.
Curiously, the data seems to become sharper at intermediate
temperatures, and then broaden again as temperature approaches 5 K.

# Transverse Magnetoresistance Hysteresis for $C_{60}:Ni_{90}$
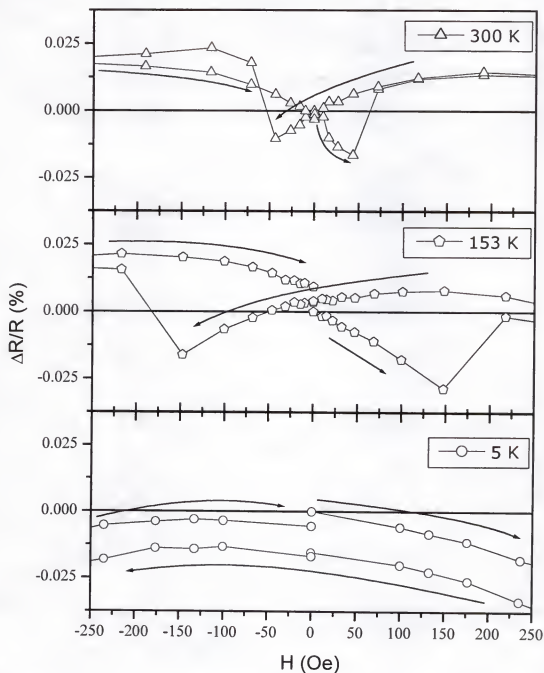


Figure 6.20    Transverse magnetoresistance for $C_{60}:Ni_{90}$, from -250–250 Oe. There is a hysteresis at low fields, which broadens, to intermediate temperatures, then disappears near the crossover from negative to positive magnetoresistance after saturation. It is possible the origin of this hysteresis lies in magnetization effects, but the cause of the disappearance at low temperatures is unknown. The arrows indicate sweep direction.

# Longitudinal Magnetoresistance for $C_{60}$:$Ni_{90}$
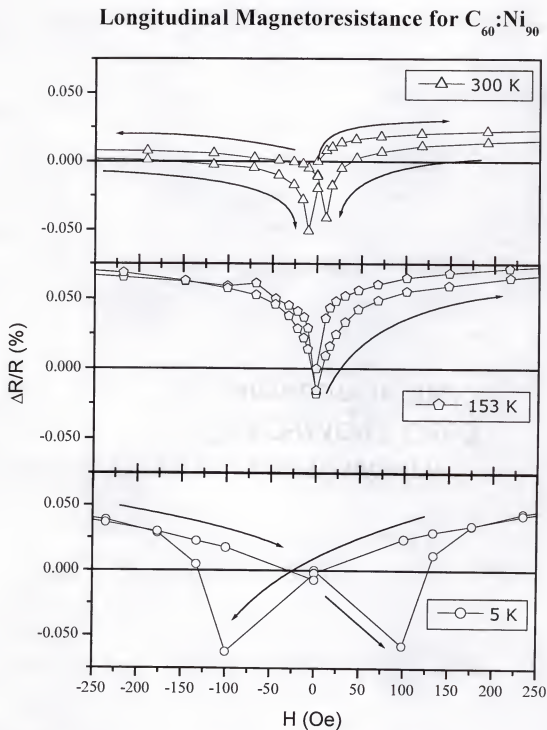


Figure 6.21    Longitudinal magnetoresistance for $C_{60}$:$Ni_{90}$ from -250–250 Oe. Note the hysteresis minima which disappear around 153 K and reappear fat lower temperatures. The peaks themselves may be accounted for by magnetization effects, but the disappearance at intermediate temperatures is not understood. The arrows indicate sweep direction.
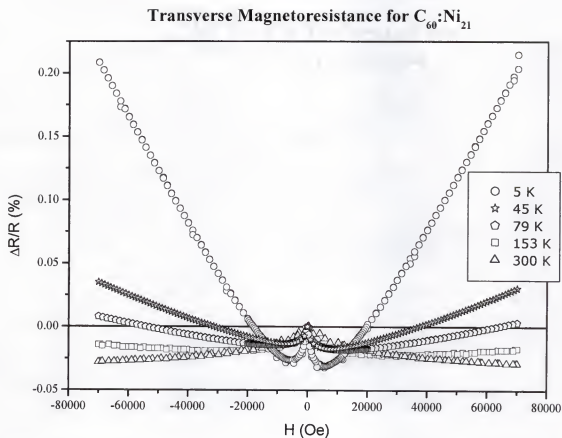
Figure 6.22    Transverse magnetoresistance for $C_{60}$:$Ni_{21}$. Note the enhancement of the anisotropic magnetoresistance effect at low fields for the 5 K data. Note also the large magnitude of the positive part of the 5 K magnetoresistance compared to that for $C_{60}$:$Ni_{90}$ and nickel.

**Longitudinal Magnetoresistance for $C_{60}$:$Ni_{21}$**
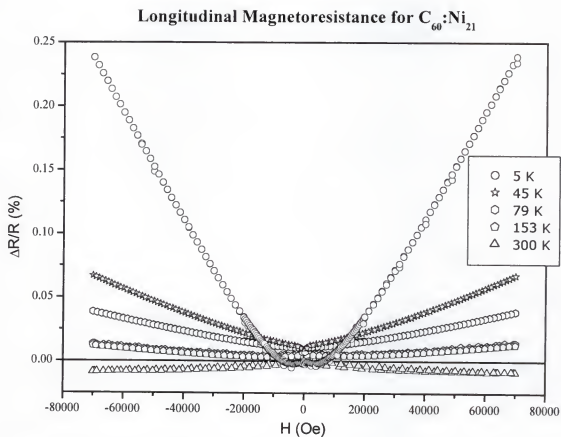
Figure 6.23    Longitudinal magnetoresistance for $C_{60}$:$Ni_{21}$. Note the suppression of the anisotropic magnetoresistance effect at 5 K, as well as the magnitude of the positive part of the magnetoresistance.

**Transverse Magnetoresistance for $C_{60}$:$Ni_{21}$**
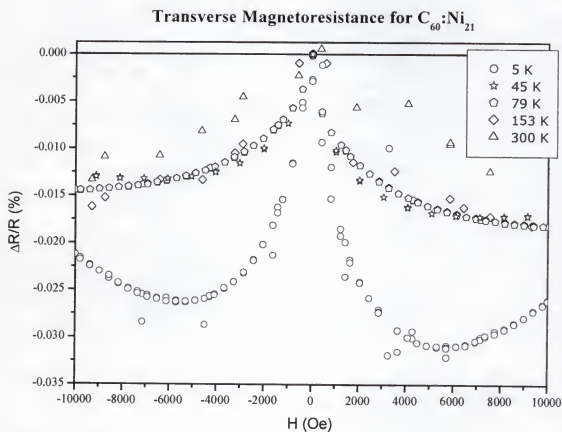
Figure 6.24    Transverse magnetoresistance for $C_{60}$:$Ni_{21}$, from -1–1 T. Note the qualitative difference between the 45 K and 5 K data. The apparent enhancement of anisotropic magnetoresistance at low fields occurs after the minimum in the $C_{60}$:$Ni_{21}$ resistance versus temperature curve.

**Longitudinal Magnetoresistance for C$_{60}$:Ni$_{21}$**
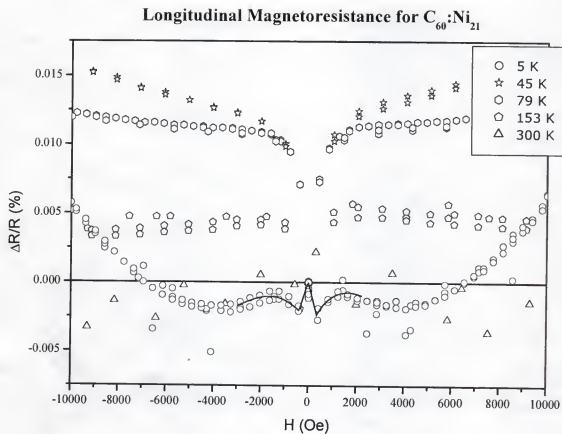
Figure 6.25  Longitudinal magnetoresistance for C$_{60}$:Ni$_{21}$, from −1–1T. At 5 K, the anisotropic magnetoresistance effect is greatly reduced, and the curve has more structure, with a sort of triple peak centered at zero field. The solid line at 5 K is a guide to the eye.

**Transverse Magnetoresistance for $C_{60}$:$Ni_{23}$**
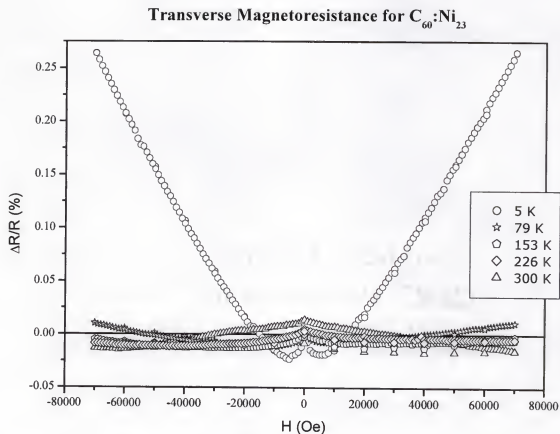


Figure 6.26    Transverse magnetoresistance for $C_{60}$:$Ni_{23}$. $C_{60}$:$Ni_{23}$'s magnetoresistance behavior is similar to that for $C_{60}$:$Ni_{21}$. The magnetoresistance is positive and much larger at 5 K than at the higher temperatures. Again, an enhancement of the anisotropic magnetoresistance is evident for the 5 K data.

# CHAPTER 7
## SUMMARY AND FUTURE DIRECTIONS

The work presented in this dissertation was performed with the goal of obtaining a better understanding of the nature of the $C_{60}$-Metal surface interaction and the electron-doped $C_{60}$ monolayer. To this end, two systems were studied: $C_{60}$/M bilayers, where the first monolayer of $C_{60}$ in contact with the metal is electron-doped by charge transfer from the metal, and $C_{60}$:$Ni_x$ composite thin films, where the $C_{60}$ host matrix separates isolated grains of nickel.

For examination of the $C_{60}$/M system, two subsystems were studied: $C_{60}$/Ni and $C_{60}$/Cu. From the change in resistance of the $C_{60}$/M as $C_{60}$ is deposited upon the surface of the metal, the sheet resistance of the conducting $C_{60}$ monolayer can be determined. It was found that the sheet resistances for $C_{60}$ electron-doped by contact with nickel and copper were approximately 59,000 and 2000 $\Omega/\square$, respectively. The large difference in sheet resistance for the two systems can be accounted for in three ways: (1) The work function of nickel (5.15 eV) is nearly equal to the energy level of $C_{60}$'s LUMO (5.2 eV); whereas, the work function of copper (4.65 eV) is far enough below $E_{LUMO}$ that the difference in $R_{\square}^{C_{60}}$ between the $C_{60}$/Ni and $C_{60}$/Cu systems could simply be due to less charge transfer between the nickel and $C_{60}$. (2) As evidenced by the near-perfect fits to a coverage model that assumes no diffusion of $C_{60}$ molecules about the surface of nickel,

there appears to be a large $C_{60}$-nickel surface interaction. There may be a hybridization of the $C_{60}$ molecular orbitals with the nickel surface orbitals, which localizes much of the transferred charge,[6, 41, 52] decreasing its mobility within the $C_{60}$ monolayer and increasing the resistance of the electron-doped monolayer. (3) The charge transfer from the nickel may have been hindered by contamination adsorbed during the warm-up of the $C_{60}$ source before $C_{60}$ deposition. Sufficient time elapsed between depositions (~5–10 min, typically) that the nickel surface could be well-covered by unwanted adsorbates. It was found that the low value of $R_{\square}^{C_{60}}$ for the $C_{60}$/Cu system could only be obtained after careful preparation of the substrate just before copper deposition and the minimization of the time between underlayer and overlayer deposition.

Transport measurements were made on one $C_{60}$/Cu bilayer sample in the ShivaStat at temperatures ranging from 2.3–250 K and in magnetic fields of up to 7 T. The bilayer film was metallic, with a roughly linear dependence on temperature, down to 55 K, where the resistance took on a -ln(T) dependence consistent with weak localization. Measurements of the magnetoresistance of the film followed roughly the form of the digamma function, also consistent with weak localization.[66, 68] From these measurements, values for the weak localization parameters $p$, and $\tau_\phi$ were obtained. After measurements of the pristine sample were made, it was exposed to air for ~30 seconds, to destroy the conductivity of the $C_{60}$ monolayer. More measurements of resistance versus temperature were then made on the exposed sample.

In weak localization theory, the ln(T) temperature dependence of the conductance has a proportionality constant $p = \alpha P$, where $\alpha$ is determined by the strengths of spin-

orbit and magnetic scattering and $P$ by the dephasing mechanism of the conduction electrons. A value for $P$ of approximately one is usually associated with electron-electron dephasing interactions.[83-85] Using Equation 3.5, a fit to the conductance versus temperature yielded $p = 0.967 \pm 0.001$ and $p = 0.713 \pm 0.001$ for the pre-vent and post-vent data, respectively. From Equation 3.4 and a fit of the form of Equation 3.6, $L_\phi$ was calculated to be 136 Å and 135 Å for 2.3 K and 4.5 K, respectively. In addition, from the magnetoconductance, values for $\alpha$ at 2.3 K and 4.5 K were determined to be 0.8 and 0.9±10%, respectively. When combined with the above-mentioned value for the pre-vent $p$, the 4.5 K $\alpha$ indicates a value for $P$ of approximately one, consistent with electron-electron interactions playing a dominant role in the $C_{60}$/Cu system. Magnet difficulties prevented the calculation of $\alpha$ for the air-exposed sample.

There are additional directions that experiments on the $C_{60}$/M system could take. Problems with the ShivaStat magnet hindered measurements of the magnetoresistance of $C_{60}$/Cu at more temperatures than 2.3 K and 4.5 K. To obtain reasonably accurate values of $L_\phi$, it is necessary to make magnetoresistance measurements over a wider range of temperatures. It would also be advantageous if one could compare the transport properties of the bilayer system to that of pure copper of the same thickness and resistivity.

For the $C_{60}$/Ni system, new samples could be grown in SHIVA where the contamination of the nickel surface by unwanted adsorbates can be minimized. In this way, one might be able to extend the region of nickel sheet resistance where the $C_{60}$ sheet resistance is constant, as well as decreasing the magnitude of the $C_{60}$ sheet resistance.

There is also the matter of transport measurements on the $C_{60}$/Ni system. It has been shown that electrons transferred to nanotubes retain their spin information on a length scale comparable to that of the tube-length.[91] This revelation raises the questions of whether the electrons transferred in the $C_{60}$/Ni system also retain their spin information, what the length scale of that retention is, and whether there is spin-dependent scattering at the $C_{60}$/M interface.

For the $C_{60}$:$Ni_x$ system, three composite samples with x = 21±2, 23±3, and 90±1 were grown, and one pure nickel sample was grown for comparison. Transport measurements were made *ex situ* in the Quantum Design PPMS, since the samples proved to be relatively air insensitive. The measurement of resistance versus temperature showed two samples (x = 21,90) that behaved metallically at high temperatures, with a turn up to insulating behavior at low temperatures. The resistance of the third sample increased slightly, roughly linearly with temperature, before turning up more sharply at low temperature. Due to the poor control of relative deposition rates for the x = 23 sample, there is more inhomogeneity, and there may be more $C_{60}$, than originally thought, which would be consistent with its insulating nature.

In Hall effect measurements, the composites are shown to be magnetic at all temperatures, with the magnetization increasing slightly with decreasing temperature. Carrier densities extracted from the linear part of the Hall resistance are in the metallic regime (~$10^{23}$ $cm^{-3}$) and are correlated with the sample resistivities. The hall mobilities, ranging from 0.25–0.4 $cm^2V^{-1}s^{-1}$ at room temperature, are very low compared to those of

typical semiconductors (ranging from 50–30000 $cm^2V^{-1}s^{-1}$at room temperature[92]), and do not seem to correlate with the resistivities.

The magnetoresistance of the composites is most intriguing. The pure nickel sample exhibits negative magnetoresistance typically associated with ferromagnetic conductors. The nickel magnetoresistance, after the saturation magnetization is reached, shows a trend to positive $\partial R/\partial H$ as the temperature decreases. For pure, clean ferromagnetic systems, it is possible at high fields and low temperatures to see a small positive magnetoresistance after $M_S$ is reached.[64], as the magnetoresistance returns to $H^2$ dependence. However, the composites show a crossover from negative to positive magnetoresistance at high temperatures, ranging from ~200 K for x = 21,23 to ~70 K for x = 90. A similar crossover in magnetoresistance is seen in Si:P just on the metallic side of the metal-insulator transition, albeit at ~1 K, which is attributed to an enhancement of Coulomb interactions through quantum mechanical interference.[90] It has been recently shown that the negative-positive magnetoresistance crossover occurs in crystalline and polycrystalline $Fe_{1-x}Co_xSi$ at temperatures around 100 K. The positive magnetoresistance in this system is also attributed to enhanced Coulomb interactions, while the high crossover temperature is associated with the large internal magnetic fields provided by the ferromagnetic dopants.[88] Though not crystalline, and fairly inhomogeneous, the $C_{60}:Ni_x$ samples are made from materials with properties similar to $Fe_{1-x}Co_xSi$. The host matrix is insulating and highly electron correlated ($C_{60}$), and the dopant is an itinerant ferromagnet. Therefore, the $C_{60}:Ni_x$ composites' magnetoresistance crossover may be due to the same mechanisms as for $Fe_{1-x}Co_xSi$.

There is much additional work that could be done to further characterize the $C_{60}:Ni_x$ composite system. The morphology of the films is unknown, and may also play an important part in the magnetoresistance. It would be useful to examine films with a wider range of stoichiometries and perform TEM measurements to discover whether the assumption that the films are composed of nickel islands in a $C_{60}$ matrix is justified. The scattering of electrons at these grain boundaries as well as the existence of the electron-doped $C_{60}$ monolayers surrounding them may have subtle roles in the crossover from negative to positive magnetoresistance.

# REFERENCES

1   H. W. Kroto, J. R. Heath, S. C. O'Brien, R. F. Curl, and R. E. Smalley, "$C_{60}$: Buckminsterfullerene," *Nature*, **318**, 162-163 (1985).

2   A. F. Hebard, R. R. Ruel, and C. B. Eom, "Charge Transfer and Surface Scattering at Cu-$C_{60}$ Planar Interfaces," *Physical Review B*, **54**, 14052 (1996).

3   E. A. Rohlfing, D. M. Cox, and A. Kaldor, "Production and Characterization of Supersonic Carbon Cluster Beams," *Journal of Chemical Physics*, **81**, 3322-3330 (1984).

4   A. F. Hebard, "Buckminsterfullerene," *Annual Reviews of Materials Science*, **23**, 159-191 (1993).

5   M. R. C. Hunt, P. Rudolf, and S. Modesti, "Photoemission and Electron-energy-loss-spectroscopy Study of $C_{60}$ Monolayers Adsorbed on Cs-precovered Au(110) and of Bulk Distilled $Cs_xC_{60}$," *Physical Review B*, **55**, 7889-7903 (1997).

6   M. R. C. Hunt, S. Modesti, P. Rudolf, and R. E. Palmer, "Charge Transfer and Structure in $C_{60}$ adsorption on Metal Surfaces," *Physical Review B*, **51**, 10039-10047 (1995).

7   B. W. Hoogenboom, R. Hesper, L. H. Tjeng, and G. A. Sawatzky, "Charge Transfer and Doping-dependent Hybridization of $C_{60}$ on Noble Metals," *Physical Review B*, **57**, 11939-11942 (1998).

8   A. J. Maxwell, P. A. Brühweiler, D. Arvanits, J. Hasselström, and N. Mårtensson, "C 1s Ionisation Potential and Energy Referencing for Solid $C_{60}$ Films on Metal Surfaces," *Chemical Physics Letters*, **260**, 71-77 (1996).

9   A. J. Maxwell, P. A. Brühweiler, A. Nilsson, N. Mårtensson, and P. Rudolf, "Photoemission, Autoionization, and X-ray-absorption Spectroscopy of Ultr-thin $C_{60}$ on Au(110)," *Physical Review B*, **49**, 10717-10725 (1994).

10  K.-D. Tsuei, J.-Y. Yuh, C.-T. Tzeng, R.-Y. Chu, S.-C. Chung, and K.-L. Tsang, "Photoemission and Photoabsorption Study of $C_{60}$ Adsorption on Cu(11) Surfaces," *Physical Review B*, **56**, 15412-15420 (1997).

11    G. K. Wertheim and D. N. E. Buchanan, "Reaction of $C_{60}$ with Metals: W," *Solid State Communications*, **88**, 97 (1993).

12    S. C. Wu, K. Xun, J. Z. Deng, J. Yao, F. Q. Liu, S. H. Lu, Z. Q. Wang, and R. S. Han, "Observation of the Development of the Electronic Structure of $C_{60}$ Films from Submonolayer Coverage of Two and Three Dimensionality," *Physical Review B*, **47**, 13830-13834 (1993).

13    W. Zhao, L.-Q. Chen, Y.-X. Li, T.-N. Zhao, Y.-Z. Huang, Z.-X. Zhang, H.-T. Wang, P.-X. Ye, and Z.-X. Zhao, "Spectroscopic Studies of the Interaction of $C_{60}$ and $C_{70}$ Films with Metal Substrates," *Spectrochemica Acta*, **50A**, 1759-1767 (1994).

14    P. J. Benning, J. L. Martins, J. H. Weaver, L. P. F. Chibante, and R. E. Smalley, "Electronic States of $K_xC_{60}$: Insulating, Metallic, and Superconducting Character," *Science*, **252**, 1417-1419 (1991).

15    C. T. Chen, L. H. Tjeng, P. Rudolf, G. Meigs, J. E. Rowe, J. Chen, J. P. M. Jr., A. B. S. III, A. R. McGhie, W. J. Romanow, and E. W. Plummer, "Electronic States and Phases of $K_xC_{60}$ from Photoemission and X-ray Absorption Spectroscopy," *Nature*, **352**, 603-605 (1991).

16    G. K. Wertheim, J. E. Rowe, D. N. E. Buchanan, E. E. Chaban, A. F. Hebard, A. R. Kortan, A. V. Makhija, and R. C. Haddon, "Photoemission Spectra and Electronic Properties of $K_xC_{60}$," *Science*, **252**, 1419-1421 (1991).

17    P. A. Brühweiler, A. J. Maxwell, A. Nilsson, N. Mårtensson, and O. Gunnarsson, "Auger and Photoelectron Study of the Hubbard $U$ in $C_{60}$, $K_3C_{60}$, and $K_6C_{60}$," *Physical Review B*, **48**, 18296-18299 (1993).

18    M. Merkel, M. Knupfer, M. S. Golden, and J. Fink, "Photoemission Study of the Electronic Structure of $C_{60}$ and $K_xC_{60}$," *Physical Review B*, **47**, 11470-11478 (1993).

19    A. F. Hebard, M. J. Rosseinsky, R. C. Haddon, D. W. Murphy, S. H. Glarum, T. T. M. Palstra, A. P. Ramirez, and A. R. Kortan, "Superconductivity at 18K in Potassium-doped $C_{60}$," *Nature*, **350**, 600-601 (1991).

20    D. W. Murphy, M. J. Rosseinsky, R. C. Haddon, A. P. Ramirez, A. F. Hebard, R. Tycko, R. M. Fleming, and G. Dabbagh, "Superconductivity in Alkali Metal Fullerides," *Physica C*, **185-189**, 403-408 (1991).

21    K. Tanigaki, T. W. Ebbesen, S. Saito, J. Mizuki, J. S. Tsai, Y. Kubo, and S. Kuroshima, "Superconductivity at 33K in $Cs_xRb_yC_{60}$," *Nature*, **352**, 222-223 (1991).

22    M. J. Rosseinsky, A. P. Ramirez, S. H. Glarum, D. W. Murphy, R. C. Haddon, A. F. Hebard, T. T. M. Palstra, A. R. Kortan, S. M. Zahurak, and A. V. Makhija, "Superconductivity in $Rb_xC_{60}$," *Physical Review Letters*, **66**, 2830-2832 (1991).

23    R. C. Haddon, A. F. Hebard, M. J. Rosseinsky, D. W. Murphy, S. J. Duclos, K. B. Lyons, B. Miller, J. M. Rosamilia, R. M. Fleming, A. R. Kortan, S. H. Glarum, A. V. Makhija, A. J. Muller, R. H. Eick, S. M. Zahurak, R. Tycko, G. Dabbagh, and F. A. Thiel, "Conducting Films of $C_{60}$ and $C_{70}$ by Alkali-metal Doping," *Nature*, **350**, 320-322 (1991).

24    S. P. Ketty, C.-C. Chen, and C. M. Lieber, "Superconductivity at 30K in Caesium-doped $C_{60}$," *Nature*, **352**, 223-224 (1991).

25    G. P. Kochanski, A. F. Hebard, R. C. Haddon, and A. T. Fiory, "Electrical Resistivity and Stoichiometry of $K_xC_{60}$ Films," *Science*, **255**, 184-186 (1992).

26    G. S. Hammond and V. J. Kuck, "Fullerenes: Synthesis, Properties, and Chemistry of Large Carbon Clusters," in *ACS Symposium Series No. 481*: American Chemical Society, 1992.

27    A. F. Hebard, "Superconductivity in Doped Fullerenes," *Physics Today*, 26-32 (1992).

28    X.-D. Xiang, J. G. Hou, G. Briceño, W. A. Vareka, R. Mostovoy, A. Zettl, V. H. Crespi, and M. L. Cohen, "Synthesis and Electronic Transport of Single Crystal $K_3C_{60}$," *Science*, **256**, 1190-1191 (1992).

29    A. F. Hebard, T. T. M. Palstra, R. C. Haddon, and R. M. Fleming, "Absence of Saturation in the Normal-state Resistivity of Thin Films of $K_3C_{60}$," *Physical Review B*, **48**, 9945-9948 (1993).

30    S. J. Duclos, R. C. Haddon, S. H. Glarum, A. F. Hebard, and K. B. Lyons, "Raman Studies of Alkali-Metal Doped $A_xC_{60}$ Films (A = Na, K, Rb, Cs; x = 0, 3, and 6)," *Science*, **254**, 1625–1627 (1991).

31    Y. Iwasa and T. Kaneyasu, "Optical Study of Electronic Structures and Phonons in Alkali-Metal-Doped $C_{60}$," *Physical Review B*, **51**, 3678–3685 (1995).

32    G. K. Wertheim, D. N. E. Buchanan, E. E. Chaban, and J. E. Rowe, "Surface Effects in Photoemission from Alkali-fullerides," *Solid State Communications*, **83**, 785-788 (1992).

33    M. S. Golden, M. Knupfer, J. Fink, J. F. Armbruster, T. R. Cummins, H. A. Romberg, M. Roth, M. Sing, M. Schmidt, and E. Sohmen, "The Electronic Structure of Fullerenes and Fullerene Compounds from High-energy Spectroscopy," *Journal of Physics: Condensed Matter*, **7**, 8219-8247 (1995).

34    T. Schedel-Neidrig, M. C. Böhm, H. Werner, J. Schulte, and R. Schlögl, "Electronic Structure of Barium-doped $C_{60}$," *Physical Review B*, **55**, 13542-13556 (1997).

35    T. Takahashi, S. Suzuki, T. Morikawa, H. Katayama-Yoshida, S. Hasegawa, H. Inokuchi, K. Seki, K. Kikuchi, S. Suzuki, K. Ikemoto, and Y. Achiba, *Physical Review Letters*, **68**, 68 (1992).

36    E. L. Shirley and S. G. Louie, "Electron Excitations in Solid C60: Energy Gap, Band Dispersions, and Effects of Orientational Disorder," *Physical Review Letters*, **71**, 133–136 (1993).

37    R. W. Lof, M. A. van Veenendaal, B. Koopmans, H. T. Jonkman, and G. A. Sawatzky, "Band Gap, Excitons, and Coulomb Interactions in Solid $C_{60}$," *Physical Review Letters*, **68**, 3924–3927 (1992).

38    A. Eilmes, R. W. Munn, B. Pac, and P. Petelenz, "Charge-transfer States and the Band Gap in Crystalline Fullerene," *Chemical Physics*, **214**, 341–349 (1997).

39    A. P. Ramirez, "$C_{60}$ and Its Superconductivity," *Superconductivity Review*, **1**, 1–101 (1994).

40    D. Varshney, M. Varshne, R. K. Singh, and R. Mishra, "Superconductivity in Alkali Metal Doped Fullerenes ($K_3C_{60}$): A Phonon Mechanism," *Journal of Physics and Chemistry of Solids*, **60**, 579–585 (1999).

41    P. W. Murray, M. Ø. Pederson, E. Lægsgaard, I. Stensgaard, and F. Besenbacher, "Growth of $C_{60}$ on Cu(110) and Ni(110) Surfaces: $C_{60}$-induced Interfacial Roughening," *Physical Review B*, **55**, 9360-9363 (1997).

42    W. B. Zhao, J. Chen, K. Wu, J. L. Zhang, C. Y. Li, D. L. Yin, Z. N. Gu, X. H. Zhou, and Z. X. Jin, "*In Situ* Electronic Transport Measurement as a Tool for Investigating the 2D Doping in Metal-$C_{60}$ Interfacial Systems," *Journal of Physics: Condensed Matter*, **6**, L631-L636 (1994).

43    X. D. Zhang, W. B. Zhao, K. Wu, Z. Y. Ye, J. L. Zhang, C. Y. Li, D. L. Yin, Z. N. Gu, X. H. Zhou, and Z. X. Jin, "Surface Enhanced Electronic Transport: A New Method to Probe the Possible Interactions Between $C_{60}$ and Non-Alkali Metals," *Chemical Physics Letters*, **228**, 100 (1994).

44    A. F. Hebard, C. B. Eom, Y. Iwasa, K. B. Lyons, G. A. Thomas, D. H. Rapkine, R. M. Fleming, R. C. Haddon, J. M. Philips, J. H. Marshall, and R. H. Eick, "Charge Transfer at Aluminim-$C_{60}$ Interfaces in Thin-film Multilayer Structures," *Physical Review B*, **50**, 17740–17743 (1994).

45    S. J. Chase, W. S. Basca, M. G. Mitch, L. J. Pilione, and J. S. Lannin, "Surface-enhanced raman Scattering and Photoemission of $C_{60}$ on Noble-metal Surfaces," *Physical Review B*, **46**, 7873-7877 (1992).

46    J. Q. Wu, W. B. Zhao, J. Chen, Z. J. Wang, J. L. Zhang, C. Y. Li, and D. L. Yin, "Nonlinear Resistivity and Critical Behavior of Metal-overlayer Percolation Systems on Epitaxial Fullerene Films," *Physical Review B*, **54**, 9840–9845 (1996).

47    X. Li, Y. J. Tang, H. W. Zhao, W. S. Zhan, H. Wang, and J. G. Hou, "Characteristic of Interface Effect in Cu-$C_{60}$ Granular Films," *Applied Physics Letters*, **77**, 984–986 (2000).

48    J. G. Hou, Y. Wang, W. Xu, S. Y. Zhang, Z. Jian, and Y. H. Zhang, "Synthesis and Characterization of Ag-$C_{60}$ Nanostructure Film," *Applied Physics Letters*, **70**, 3110–3112 (1997).

49    P. Wißmann, The Electrical Resistivity of Pure and Gas Covered Metal Films, pp. vol. 77, Springer Verlag, (1975).

50    D. Schumacher, Surface Scattering Experiments with Conduction Electrons, pp. vol. 128, New York, Springer-Verlag, (1993).

51    L. Q. Jiang and B. E. Koel, "Charge Transfer from Potassium into the $t_{1g}$ Band of $C_{60}$," *Physical Review Letters*, **72**, 140-143 (1994).

52    C. Cepek, A. Goldoni, and S. Modesti, "Chemisorption and Fragmentation of $C_{60}$ on Pt(111) and Ni(110)," *Physical Review B*, **53**, 7466-7472 (1996).

53    K. Motai, T. Hashizume, H. Shinohara, Y. Saito, H. W. Pickering, Y. Nishina, and T. Sakurai, "$C_{60}$ Growth on the Cu(111)1×1 Surface," *Japanese Journal of Applied Physics*, **32**, L450-L453 (1993).

54    W. Zhao, K. Luo, J. Chen, J. Zhang, C. Li, D. Yin, Z. Gu, X. Zhou, and Z. Jin, "Study of Microstructure and Anomalous Variation of Resistivity in Metal-$C_{60}$ Multilayer Thin Films," *Solid State Communications*, **83**, 853-855 (1992).

55    W. Zhao, K. Luo, J. Chen, C. Li, D. Yin, Z. Gu, X. Zhou, and Z. Jin, "A Possible interaction Between Non-Alkali Metals and $C_{60}$ Thin Films," *Journal of Physics: Condensed Matter*, **4**, L513-L514 (1992).

56    A. B. Pippard, <u>Magnetoresistance in Metals</u>, Cambridge University Press, (1989).

57    R. C. O'Handley, "Hall Effect Formulae and Units," in *The Hall Effect and Its Applications*, C. L. Chien and C. R. Westgate, Eds. New York, Plenum Press, 1980, pp. 417.

58    L. Berger and G. Bergmann, "The Hall Effect of Ferromagnets," in *The Hall Effect and It's Applications*, C. L. Chien and C. R. Westgate, Eds. New York, Plenum, 1980.

59    C. M. Hurd, <u>The Hall Effect in Metals and Alloys</u>, pp.,, New York, Plenum Press, (1972).

60    W. A. Reed and E. Fawcett, "High-field Galvanomagnetic Properties of Metals," *Science*, **146**, 603-610 (1964).

61    A. B. Pippard, "Longitudinal Magnetoresistance," *Proceedings of the Royal Society of London, Series A, Mathematical and Physical Sciences*, **282**, 464-484 (1964).

62    J. L. Olsen, "Galvaonomagnetic Effects (Chapter 3)," in *Electron Transport in Metals*, Interscience Publishers, a division of John Wiley & Sons, Inc., 1962.

63    N. W. Ashcroft and N. D. Mermin, <u>Solid State Physics</u>, pp. 229-239, first ed, Saunders College, (1976).

64    T. R. McGuire and R. I. Potter, "Anisotropic Magnetoresistance in Ferromagnetic 3d Alloys," *IEEE Transactions on Magnetics*, **MAG-11**, 1018–1038 (1975).

65    J. Smit, "Magnetoresistance of Ferromagnetic Metals and Alloys at Low Temperatures," *Physica*, **16**, 612–627 (1951).

66    G. Bergmann, "Consistent Temperature and Field Dependence in Weak Localization," *Physical Review B*, **28**, 515–522 (1983).

67    P. W. Anderson, E. Abrahams, and T. V. Ramakrishnan, "Possible Explanation of Nonlinear Conductivity in Thin-Film Metal Wires," *Physical Review Letters*, **43**, 718–720 (1979).

68    S. B. Arnason, Private communication, (2001).

69    F. Komori, S.-i. Kobayashi, Y. Ootuka, and W. Sasaki, "Experimental Study of Electron Localization in a Two-Dimensional Metal," *Journal of the Physical Society of Japan*, **50**, 1051–1052 (1981).

70    S. Hikami, A. I. Larkin, and Y. Nagaoka, "Spin-Orbit Interaction and Magnetoresistance in the Two Dimensional Random System," *Progress on Theoretical Physics*, **63**, 707–710 (1980).

71    G. Bergmann, "Physical Interpretation of Weak Localization: A Time-of-flight Experiment with Conduction Electrons," *Physical Review B*, **28**, 2914–2920 (1983).

72    B. L. Al'tschuler, D. Khmel'nitzkii, A. I. Larkin, and P. A. Lee, "Magnetoresistance and Hall Effect in a Disordered Two-Dimensional Electron Gas," *Physical Review B*, **22**, 5142–5153 (1980).

73    T. Hiraoka, "Hall Effect and the Pressure Effect in Single Crystals of Nickel," *Journal of Science of the Hiroshima University, Ser. A-II*, **32**, 153 (1968).

74    N. Rostoker and E. M. Pugh, "On the Hall Effect in Ferromagnets," *Physical Review*, **82**, 125 (1951).

75    Y. Kuk, D. K. Kim, Y. D. Suh, H. P. Park, S. J. Oh, and S. K. Kim, "Stressed $C_{60}$ Layers on Au(001)," *Physical Review Letters*, **70**, 1948-1951 (1993).

76    H. Xu, D. M. Chen, and W. N. Creager, "Double Domain Solid $C_{60}$ on Si(111)7×7," *Physical Review Letters*, **70**, 1850-1853 (1993).

77    E. I. Altman and R. J. Colton, "Nucleation, Growth, and Structure of Fullerene Films on Au(111)," *Surface Science*, **279**, 49-67 (1992).

78    Y. Z. Li, J. C. Patrin, M. Chander, J. H. Weaver, L. P. F. Chibante, and R. E. Smalley, "Ordered Overlayers of $C_{60}$ on GaAs(110) Studied with Scanning Tunneling Microscopy," *Science*, **252**, 547-548 (1991).

79    K. T. McCarthy, Private communication, (2000).

80    M. Pedio, K. Hevesi, N. Zema, M. Capozi, P. Perfetti, R. Gouttebaron, J.-J. Pireaux, R. Caudano, and P. Rudolf, "$C_{60}$/Metal Surfaces: Adsorption and Decomposition," *Surface Science*, **437**, 249–260 (1999).

81    M. D. Upward, P. Moriarty, and P. H. Beton, "Double domain Ordering and Selective Removal of C60 on Ag/Si(111)–($\sqrt{3}\times\sqrt{3}$)$R30°$," *Physical Review B*, **56**, R1704–R1707 (1997).

82    T. Hashizume and T. Sakurai, "FI-STM Study of Fullerenes," *Materials Research Society Symposium Proceedings*, **349**, 171–183 (1994).

83    A. G. Aronov, M. E. Gershenzon, and Y. E. Zhuralev, "Quantum Effects in Percolation Systems. Granular $Cu_{1-x}O_x$ Films," *Soviet Physics JETP*, **60**, 554–563 (1984).

84    L. A. Zheng, B. M. Lairson, and E. V. Barrera, "Formation of Nanomagnetic Thin Films by Dispersed Fullerenes," *Applied Physics Letters*, **77**, 3242-3244 (2000).

85    I. A. Campbell and A. Fert, "Transport Properties of Ferromagnets," in *Ferromagnetic Materials*, vol. 3, E. P. Wohlfarth, Ed. Amsterdam, North-Holland, 1982, pp. 747-804.

86    N. Manyala, Y. Sidis, J. F. DiTusa, G. Aeppli, D. P. Young, and Z. Fisk, "Magnetoresistance from Quantum Interference Effects in Ferromagnets," *Nature*, **404**, 581-584 (2000).

87    A. Frydman, T. L. Kirk, and R. C. Dynes, "Superparamagnetism in Discontinuous Ni Films," *Solid State Communications*, **114**, 481–486 (2000).

88    T. F. Rosenbaum, R. F. Milligan, M. A. Paalanen, G. A. Thomas, and R. N. Bhatt, "Metal-Insulator Transition in a Doped Semiconductor," *Physical Review B*, **27**, 7509-7523 (1983).

89    K. Tsukagoshi, B. W. Alphenaar, and H. Ago, "Coherent Transport of Electron Spin in a Ferromagnetically Contacted Carbon Nanotube," *Nature*, **401**, 572-574 (1999).

90    C. Kittel, Introduction to Solid State Physics, pp. 220–221, 7th ed, New York, John Wiley & Sons, Inc., (1996).

91    L. M. Hughes, Private Communication, (2000).

BIOGRAPHICAL SKETCH

Quentin Michael Hudspeth was born the first child of Mr. Clark Davis Hudspeth and Mrs. Lorita Marie Hughes on September 30, 1971 in Gonzales, Louisiana. It has been said by his parents that nearly as soon as he could focus his eyes, he began mentally devouring all new items, scrutinizing them as though trying to figure out how they worked.[93] As far as he can remember, he has always wanted to know what made things tick. This desire to understand the workings of the universe was indulged angelically by his parents, who had (and still have) to endure endless questions of why and how on subjects ranging from cooking to welding.

His grade school and high school years were fairly uneventful. In fourth grade, when his grades began to drop, he was diagnosed with boredom, and enrolled in the Talented and Gifted (TAG) program. From then until eighth grade, he was enrolled in an extra class that indulged his scientific interests. He was introduced to concepts like the scientific method and computers several years before the 'average' students. The TAG class also gave him an opportunity to make like-minded friends and indulge his imaginative and creative side. Like many boys his age, during these years he rapaciously went through the school library's dinosaur collection, then started in on space science and science fiction. His head, as they say, was in the stars.

High school flew by quickly, and Quentin graduated 13th in his class in May of 1989. Now it was time to pick a college. A strong desire to get out of state (influenced to

a great degree by being the only one of his circle of friends to be moving on to college), decided him to accept a small scholarship from Mississippi State University. The choice of a major, however, was not a simple one. Having for some time thought he would like to be either an astronaut or a writer, he joined the physics department, with the idea of maybe becoming a mission specialist. Besides, he always did like to know how things worked.

Quentin soon discovered that he quite enjoyed his physics classes, and wasn't a bad hand at solving problems, either. In the spring of his sophomore year, he earned the distinction of becoming the youngest student to teach laboratory classes in the physics department (they were running low on graduate students). Soon he discovered a talent for and enjoyment of teaching. He continued to teach various lab courses during his undergraduate career. As a participant in the Department of Energy Science and Engineering Research Semester, Quentin spent the spring semester of his fourth undergraduate year at Los Alamos National Laboratory in Los Alamos, New Mexico in the Space Science Technology (SST) Division. Under the guidance of Morris Pongratz, Quentin worked on modifying and debugging a FORTRAN Monte-Carlo program for modeling the flight path of a cloud of barium ions in the upper ionosphere. During this program, Quentin met his future wife, Heather Lynn, who was also enrolled in the program. For the next two summers, he continued working at Los Alamos in the SST Division. During his fifth, and final, year at MSU, he worked for Patrick Lestrade, analyzing Gamma Ray Burst data from the BATSE detector on the Compton Gamma Ray Observatory.
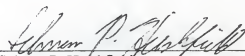
In the spring of 1994, Quentin graduated cum laude with a B.S. in physics. The following fall he began his graduate studies at the University of Florida's Department of Physics. Still with his head in the stars, his first year there was spent teaching, taking core courses and trying to find a niche in the Astrophysics group. That summer, on the best Saturday of his life, May 20, 1995, he married Heather. In the fall of 1995, he continued teaching and pursuing courses for a career in cosmology. However, he found himself increasingly uncomfortable with what such a career might entail. Under the advice of his wife and friends in the Condensed Matter Experiment group, he signed on with Art Hebard—newly arrived from Bell Labs—for an experimental semester of lab work in the spring of 1996. He was soon hooked, and put aside his pocket protector for a tool belt. While completing the work reported herein, Quentin took the opportunity to familiarize himself with tunneling-electron and scanning-electron microscopes, photolithography and any other equipment his experimentalist friends would take time to explain to him. He also earned a brown sash in Shaolin kung fu, and learned to play the guitar (two chords, anyway).

I certify that I have read this study and that in my opinion it conforms to acceptable standards of scholarly presentation and is fully adequate, in scope and quality, as a dissertation for the degree of Doctor of Philosophy.

Arthur F. Hebard, Chairman
Professor of Physics

I certify that I have read this study and that in my opinion it conforms to acceptable standards of scholarly presentation and is fully adequate, in scope and quality, as a dissertation for the degree of Doctor of Philosophy.

Selman P. Hershfield
Associate Professor of Physics

I certify that I have read this study and that in my opinion it conforms to acceptable standards of scholarly presentation and is fully adequate, in scope and quality, as a dissertation for the degree of Doctor of Philosophy.
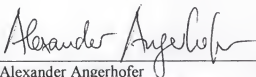
Fred Sharifi
Associate Professor of Physics

I certify that I have read this study and that in my opinion it conforms to acceptable standards of scholarly presentation and is fully adequate, in scope and quality, as a dissertation for the degree of Doctor of Philosophy.

Mark W. Meisel
Professor of Physics

I certify that I have read this study and that in my opinion it conforms to acceptable standards of scholarly presentation and is fully adequate, in scope and quality, as a dissertation for the degree of Doctor of Philosophy.

Alexander Angerhofer
Associate Professor of Chemistry

This dissertation was submitted to the Graduate Faculty of the Department of Physics in the College of Liberal Arts and Sciences and to the Graduate School and was accepted as partial fulfillment of the requirements for the degree of Doctor of Philosophy.

May 2001

Dean, Graduate School